universität wien

MASTERARBEIT / MASTER'S THESIS

Titel der Masterarbeit / Title of the Master's Thesis

„Absorption Imaging of a Bose-Einstein Condensate“

verfasst von / submitted by

Claudia Heindler, B.Sc.

angestrebter akademischer Grad / in partial fulfilment of the requirements for the degree of

Master of Sience (M.Sc.)

Wien, 2018 / Vienna, 2018

Studienkennzahl lt. Studienblatt / degree programme code as it appears on the student record sheet:	A 066 876
Studienrichtung lt. Studienblatt / degree programme as it appears on the student record sheet:	Masterstudium Physik
Betreut von / Supervisor:	o. Univ.-Prof. Dr. Anton Zeilinger

Acknowledgments

First of all, I want to thank Professor Zeilinger for giving me the opportunity to work with him and be part of his research group at the IQOQI Vienna. He gave me the chance to be a full part of the research group. During my year at the institute I met so many outstanding people, which were not only part of my everyday work but with whom I also enjoyed the time outside the lab.
I am particularly grateful for the support given by my supervisors Michael Keller and Kahan Dare who welcomed me with open arms in their team right from the beginning. Thanks for being always patient with me and answering all my questions – even if it was the same question over and over again.
Nevertheless, I would not have come to this point without my friends Flo, Martin, Thomas, Tobi and Georg. Most of my physics knowledge was developed and gained within the years of studying together with you. Thank you for all the valuable discussions about physics and for always encouraging me to give my best. I also want to thank Georg and Flo for reading this thesis and adding their comments to my work.
Finally, special thanks to my family and all my friends who always supported me and never stopped believing in what I was doing.

Abstract

This master thesis aims on characterizing a Bose-Einstein condensate of metastbale helium atoms, which is created in a crossed optical dipole trap (ODT). By providing a coherent matter wave, the BEC is expected to allow the generation of the originally proposed EPR state of massive particles entangled in their external degrees of freedom: momentum and position. For characterizing the BEC, it is important to gain detailed knowledge of the optical dipole trap. For this, the trap frequencies of the latter are measured by the method of parametric excitation. This is done by periodically varying the trap depth in the dipole trap. When the frequency of this variation is in resonance with the trap frequency, energy is pumped into the system. This leads to heating of the atoms, which thus escape from the trap. These trap losses can be detected via absorption imaging of the atoms. Absorption imaging is crucial for getting information about the density and atom number of the BEC. Thus, within this thesis a new absorption imaging setup was implemented and investigated. This setup consists of a new camera as well as an improved lens system. Previously, an EMCCD[1] camera was used for imaging the atomic cloud. To do this, the atomic cloud is illuminated with resonant 1083 nm infrared light. However the camera exhibits a quantum efficiency of significantly less than 1% in this wavelength regime. This results in noisy images of the atomic cloud which lead to limitations for further investigations with this imaging system. Therefore, in the framework of this thesis, a new camera was bought. The Cheetah 110Hz camera belongs to the class of InGaAs (indium-gallium-arsenide) cameras. The sensor, made out of the afore mentioned semi-conducting material, provides a quantum efficiency of $\sim 70\%$ in the infrared regime and is therefore a promising alternative to the EMCCD camera. However, not only does the camera provide restrictions on the possibilities of the imaging system but also the imaging lens. The previous lens was designed such that the cloud gets demagnified by a factor of 4, leading to a reduction in resolution. Thus, an alternative lens system offering a magnification of $M \approx 2$ was designed and investigated. In order to improve this imaging system further, a new type of lens was considered - so called telecentric lenses. Two such lenses were bought, one offering a magnification of $M = 1.85$ and the other one with a magnification of $M = 0.28$. These lenses enable magnification, independent of the object distance and therefore do not exhibit unintended effects such as distortion[2]. This new absorption imaging system was then used for analyzing the measurements of the parametric excitation of the optical dipole trap. This trap,

[1] electron-multiplying charge coupled device

[2] Unfortunately the lead time of the $M = 1.85$ lens exceeds the time line of this thesis and is therefore not taken into account within this thesis.

which provides a 3D trapping potential, consists of two intersecting laser beams. One of the beams propagates in horizontal direction, the other one in vertical direction. In order to measure the trap frequencies, the potentials provided by the two beams were varied separately. This enabled to assign the three measured trap frequencies to the three different spacial directions. With those results, characteristic quantities like size, density, chemical potential and temperature of the BEC were calculated. Thus, important fundamental information about the condensate but also about the dipole trap were gained within this thesis.

Zusammenfassung

Das Ziel dieser Masterarbeit ist die Charakterisierung eines Bose-Einstein Kondensats, welches in einer optischen Dipolfalle erzeugt wird. Mit Hilfe dieser kohärenten Materiewelle soll es der Forschungsgruppe gelingen, den ursprünglich von Einstein, Podolsky und Rosen vorgeschlagenen verschränkten Zustand von massereichen Teilchen zu generieren: Verschränkung in den externen Freiheitsgraden Ort und Impuls der Teilchen. Um das zu erreichen, ist es wichtig, über genügend Informationen über das Bose-Einstein Kondensat zu verfügen. Dafür wiederum ist es nötig, die optische Dipolfall, in der es erzeugt wird, zu untersuchen und zu charakterisieren. Um das zu erreichen, werden die Eigenfrequenzen der Fall ("trapping frequencies") mittels parametrischer Anregung bestimmt. Das beduetet, dass die Tiefe des Dipolfallenpotenzials periodisch variert wird. Ist die Frequenz dieser Variation in Resonanz mit der Eigenfrequenz der Falle, so wird dem System Energie zugeführt. Diese Energie führt zum Erwären der Atome (in Form von zusätzlicher kinetischer Energie). Als Folge davon besitzen die Atome genügend Energie, um das Fallenpotenzial zu überwinden und aus der Falle auszutreten. Diese Fallenverluste bzw. diese Abnahmen der Atomzahl können mittels Absorptionsabbildung ("absorption imaging") analysiert werden. Somit ist das Verfahren der Absorptionsabbildung essentiell, um Informationen über die Atomwolke und somit auch die Falle zu erhalten.
Aufgrunddessen wurde im Rahmen dieser Arbeit ein neues Absorptionsabbildungssystem entwickelt und am Experiment eingebaut. Dieses neue System besteht aus einer neuen Kamera sowie einem neuen Linsensystem. Bisher wurde eine EMCCD[1] Kamera verwendet, um die Atomwolke abzubilden. Für die Detektion müssen die Atome mit resonantem Laserlicht beleuchtet werden. Diese resonanten Wellenlänge befindet sich allerdings mit 1083 nm im Infrarotbereich. In diesem Bereich weist die EMCCD Kamera jedoch nur eine Quanteneffizienz von weniger als 1% auf. Das hat sstark verrauschte Bilder zur Folge und limitiert somit die Möglichkeiten des Abbildungsverfahrens. Aufgrunddessen wurde im Rahmen dieser Arbeit eine neue Kamera gekauft: die Cheetah 110Hz Kamera. Diese gehört zum Typ der InGaAs (Indium-Gallium-Arsenid) Kameras. Dieses Halbleitermaterial weist eine Quanteneffizienz von etwa 70% im Infrarotbereich auf und stellt somit eine vielsprechende Alternative zum bisher verwendeten Kameratyp dar. Allerdings wird die Qualität des Detektionssystems nicht nur von der Kamera, sondern auch vom verwendeten Linsensystem bestimmt. Die bisher verwendete Linse hat das Bild um ca. 1/4 verkleinert, was das Auflösungsvermögen limitiert. Deshalb wurde ein alternatives Linsensystem entworfen, das eine Vergrößung um den Faktor ~ 2 bietet. Beim Testen dieses Abbildungssystems wurde festgestellt, dass es zu starken Verzerrungen des Bildes

kommt. Das kann gerade am Rande des Sichtfeldes zu falschen Größenverhältnissen des Bildes führen. Deshalb wurde beschlossen, das Linsensystem zu verbessen, indem anstelle von herkömmlichen Linsen ein sogenanntes Telezentrisches Linsensystem verwendet wird. Diese ermöglichen eine Vergößerung des Abbildungsobjektes unabhängig vom Abstand zwischen Objekt und Linse. Dadurch werden unerwünschte Effekte wie z.B. Verzerrungen minimiert. Zwei solcher Linsensysteme wurden gekauft, eines ermöglicht eine Verkleinerung des Bildes um ca. 1/4, während das andere eine Vergrößerung um den Faktor ~ 2 bietet[3].
Mit Hilfe dieses neuen Abbildungssystems wurden die Messungen der parametrischen Anregung der optischen Dipolfalle analysiert. Diese Falle, die ein drei dimensionales Potenzial zu Verfügung stellt, besteht aus zwei gekreuzten Laserstrahlen, einem horizontal und einem veritkal verlaufenden Laserstrahl. Um die Frequenzen der Falle zu vermessen, wurden die Fallenpotenziale dieser beiden Strahlen jeweils separat variiert. Somit war es möglich, die drei gemessenen Frequenzen den jeweiligen Raumrichtungen zuzuordnen. Mit diesen Ergebnissen wurden dann charakteristische Größen des Bose-Einstein Kondensats berechnet, wie z.B. Größe, Dichte, chemisches Potenzial und Temperatur. Es konnten somit grundlegende, neue Informationen über das Kondensat aber auch die Dipolfalle gewonnen werden.

[3]Die Lieferzeit dieses Objektivs übersteigt jedoch den Zeitrahmen dieser Masterarbeit und kann somit hier nicht näher berücksichtigt werden.

Contents

Chapter 1 Introduction

1.1 Motivation

More than 100 years ago, in 1900, Max Planck introduced the pioneering idea of discrete portions of energy in order to describe black-body radiation. Only 5 years later, Albert Einstein further developed Planck's idea to the concept of light quanta of electromagnetic radiation – so called photons. For his leading work, Einstein received the Nobel Prize in 1921. Niels Bohr further applied the idea of quantized energy to the atom, explaining stability of the atom as well as spectral lines of atoms. Not only the quantization of physical variables but also experiments like Thomas Young's double slit, showing the wave-particle duality of light, were crucial for the development of modern quantum mechanics. Louis de Broglie postulated that not only light but matter in general demonstrates wave and particle characteristics at the same time, leading to the concept of so called matter-waves. Further quantum mechanical phenomena as the Pauli exclusion principle as well as Bose-Einstein and Fermi-Dirac statistics were formulated in the following years. The physical theory was completed with a fully consistent mathematical description of quantum mechanics developed by Heisenberg and Schrödinger independently.

In 1935, Albert Einstein, Boris Podolsky and Nathan Rosen (EPR) formulated a gedankenexperiment, also known as EPR paradox, arguing the incompleteness of the quantum mechanical description of physical reality, leaving open the question if a complete description does exist at all. In their original work, they adressed this question in terms of the two conjugate variables momentum and position of two freely moving massive particles [1]. The EPR paper led to strong debates in the physics community of the time. Erwin Schrödinger in a response to the EPR paper was the first one calling the two interacting systems "entangled" [2]. The argument of Einstein, Podolsky and Rosen was restated to spin observables by David Bohm in 1957 [3] and John Bell in 1964 [4] formulated an inequality (today known as Bell's inequality), which, if violated, proofs quantum entanglement. So far, several experiments were done, proving and investigating entanglement in many physical system. However, the originally proposed EPR states have not been realized experimentally. The main reason for that are decoherence effects of massive particles resulting from the strong coupling to the environment. Perrin et al. [5] suggested that Bose-Einstein condensates (BECs) of metastable helium, serving as source of coherent matter waves, could finally lead to experimental realization of EPR states as single atoms of noble gases can efficiently be detected due to their high internal energy. Bose-Einstein condensates were theorized in 1925 by Satyendra Nath Bose [6] and Albert Einstein [7], pre-

dicting that identical integer spin particles would collapse into a single quantum state at low enough energies. First experimental realizations of BECs were possible 70 years later, with the use of laser-cooling techniques[8, 9]. After another 10 years, in 2001, first metastable helium Bose-Einstein condensates were experimentally realized [10, 11] and have been extended to single-particle detection experiments during the following years. This led to the possibility of performing matter-wave experiments [12, 13], based on four-wave mixing (FWM) [14] in analogy to leading photon-entanglement experiments [15, 16] using spontaneous parametric down-conversion (SPDC) for creating entangled photon pairs. Such matter-wave experiments based on FWM combined with single-atom detection reveal correlations that even exceed the classical ones [17]. All these discoveries reinforce the suggestion that metastable helium BECs are a promising candidate for producing the originally proposed EPR states for massive particles. These states would open up a novel playground for pioneering atom experiments where entanglement in matter-waves and influence of gravity on entangled states can be further investigated.

1.2 Outline of the Thesis

In Chapter (2) the experimental setup for producing a Bose-Einstein condensate of metastable helium is introduced. In order to create a BEC, several steps of manipulating the atoms have to be done, including laser cooling methods and trapping of the atoms in commonly used traps for ultra-cold atoms.
Chapter (3) focuses on the technique of absorption imaging and the imaging system needed for this detection method. The current imaging system is investigated and compared with the newly designed system. For this, test measurements with the newly bought Cheetah 110Hz camera, consisting of an indium-gallium-arsenide (InGaAs) sensor, were done. This sensor type offers a quantum efficiency[4] of $\sim 70\%$ in the infrared regime whereas the current EMCCD camera provides significantly less than 1 % in this wavelength regime. Noise behavior of the cameras is investigated and compared. Further, the newly bought telecentric lens for the imaging system is compared with the current lens. These tests showed that the first lens indeed performs much better, as it shows minimal unintended distortion of the image. In Chapter (4), the crossed optical dipole is characterized by the method of parametric excitation. The results for the measured trapping frequencies of the trap are presented and used for further characterization of the BEC: chemical potential, size of the cloud, mean density and mean free path are calculated.

[4] This is the ratio of incident photons to converted electrons on a sensor.

Chapter 2 Overview of the Experimental Setup

This chapter provides a short overview of the experimental setup and the methods used in order to produce a Bose-Einstein condensate (BEC). A detailed theoretical description of every experimental step is omitted at this point. Nevertheless, the important steps for this thesis can be found in the respective chapters.
The experiment consists of a He*-source, a collimation region followed by a Zeeman slower for cooling and three different ultra-cold atom traps: a magneto-optical trap, a magnetic trap, and an optical dipole trap. Detection of the atoms is done either via absorption imaging or with a delay line detector. Figure (1) shows these components in different colors and gives a schemtic overview of the setup [18].

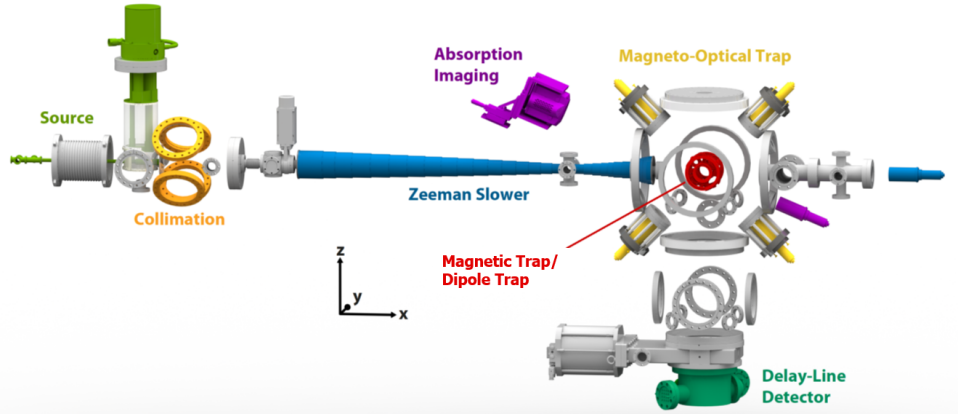

Figure 1: A schematic sketch of the experimental set up is shown. The source produces a metastable ^{4}He-beam. This beam is collimated in the collimation region via transverse laser cooling before it enters the Zeeman slower which decelerates the atomic beam. This makes it possible to trap and cool the atoms in the magneto-optical trap. Further cooling of the atomic cloud is done in the magnetic trap. As a last step towards a BEC, the atoms get loaded into the crossed optical dipole trap, whose trap center overlaps with the center of the magnetic trap. Detection of the atoms is possible either via absorption imaging or with the delay-line detector [18].

2.1 The Source: Metastable Helium - Properties and Production

In contrast to other BEC experiments [9, 19, 20], ^{4}He in its first excited state 2^3S_1 (metastable He - also denoted as He*) is used in order to produce a BEC. This isotope of helium, the second lightest element, has a natural abundance of 99.99986% and a mass of 4.002 603 254 153(64) amu [21]. As direct photon transitions[5] from this 2^3S_1 triplet state to the 1^1S_0 ground-state are doubly forbidden due to quantum-mechanical selection rules [6], metastable He has a lifetime of 7870(510) seconds which make it the longest-lived neutral atom state. It therefore acts as an effective ground-state in the experiment, as one experimental run takes about 5 to 7 seconds. Transitions to the 2^3P_2 level can be driven with 1083 nm laser light, as represented in Figure (2). For this experiment, the most beneficial property of this atomic state is its high internal energy: almost 20 eV make it the most energetic metastable state of any atomic species [22] and allow for single-atom detection. The reason for this is the release of this high internal energy via Penning ionization when the metastable He atom collides with any other atom [23]. The results of this process are the deexcitation of He* to the ground-state, the ionization of the other particle and a free electron. This can not only happen between He* atoms and other particles but also between He* atoms themselves. Another important physical quantity for describing structure and dynamics of a BEC is the s-wave scattering length a, characterizing interactions between two ultra-cold atoms. For He* this has a value of $a = (7.512 \pm 0.005)$ nm [24]. The atomic transitions which are important for this experiment [25] are shown in Figure (2) and listed in the following Table (1).

Atomic Transition	**Resonant Wavelength**	**Linewidth [MHz]**	**Saturation Intensity [mWcm^{-2}]**
$2^3S_1 \rightarrow 2^3P_{0,1,2}$	1083 nm	$\Gamma = 2\pi \cdot 1.62$	$I_{\text{sat}} = 0.16$
$2^3S_1 \rightarrow 3^3P_{0,1,2}$	389 nm	$\Gamma = 2\pi \cdot 1.49$	$I_{\text{sat}} = 3.31$

Table 1: Optically accessible atomic states of helium relevant to the experiment.

[5] A direct photon transition is an excitation or de-excitation due to the absorption or emittance of a resonant photon.

[6] The two selection rules which would need to be broken are: $\Delta l = \pm 1$ and a spin flip of one of the two electrons.

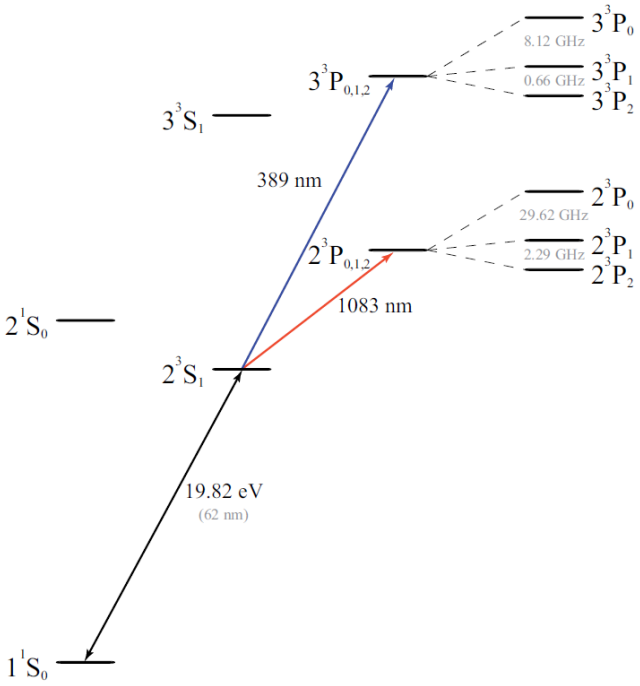

Figure 2: The energy levels of metastable helium [25]. The first excited state 2^3S_1 with an internal energy of 19.82 eV serves as an effective ground-state for the experiment as it offers a lifetime of $\sim$ 7870 seconds. With a 1083 nm laser, transitions to the $2^3P_{0,1,2}$ triplet state can be driven, whereas with 389 nm laser light the $3^3P_{0,1,2}$ states are optically accessible.

As already mentioned, optical transitions from the ground-state to the metastable state are doubly forbidden, resulting in the need to generate a plasma to access the metastable state. In order to do so, ultra pure helium enters the vacuum chamber of the supersonic cold cathode discharge source (shown in Figure (3)). The gas flows to the cold finger which is held at 17 K with a cryostat to pre-cool the helium from room temperature. Between the tungsten needle and the nozzle, the atoms enter a strong electric field (2 kV). As a result, some of the atoms are ionized and start forming a plasma, the rest is pumped out of the system. Recombinations of helium ions with free electrons lead to neutral helium atoms in different electronically excited states. A fraction of the atoms also ends up in the 2^3S_1 metastable state. The about 1 cm long expansion region after the nozzle is followed by a conically shaped skimmer for pre-collimation of the atomic beam. The latter transmits He* but also photons, ions and other ^{4}He states into the high vacuum chamber. The source is usually operated with a DC voltage of 2 kV and an helium inlet pressure of 3 mbar resulting in $4 \cdot 10^{14}$ atoms $\cdot\, \mathrm{sr}^{-1} \cdot \mathrm{s}^{-1}$ with a velocity of 800 m $\cdot\, \mathrm{s}^{-1}$ [26].

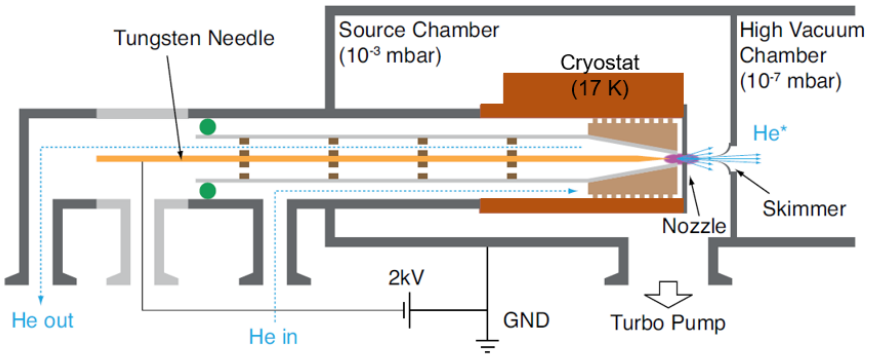

Figure 3: Schematic diagram of the metastable helium source. Ultra pure helium enters the system and is pre-cooled to ~ 17 K with a cryostat. When entering the high voltage region (2 kV) between a tungsten needle and the nozzle, some of the atoms form a plasma in which, due to recombination, a small fraction ends up in the metastable state. Through a skimmer, a pre-collimated atomic beam enters the high vacuum chamber [25].

2.2 Collimation of a He*-Beam

After the skimmer, the atomic beam is still highly divergent and only a small fraction would reach a trap at the end of the 2 m long experimental setup. Hence, as a next step of collimation, two-dimensional laser cooling is implemented. For this, 1083 nm resonant laser light is used. With that, only He* atoms are addressed by the laser beam. Collimation is realized with curved wavefronts [27]. The latter are achieved by locally different wave vectors $\vec{k}_L$ of a collimated laser beam. When atoms move with velocity $\vec{v}_A$, the frequency of the laser light observed by the atoms is Doppler shifted by δ_D:

$$\delta_D = -\vec{k}_L \cdot \vec{v}_A = -k_L \cdot v_A \cdot \cos\theta \,, \tag{1}$$

where θ is the angle between $\vec{k}_L$ and $\vec{v}_A$. Equation (1) shows the angle dependence of the Doppler shift. The curved wavefronts prevent atoms from falling out of resonance. For this, two orthogonal linearly polarized 1083 nm beams enter the vacuum system directly after the skimmer under a certain angle β. The beams are reflected between two mirror pairs, where each mirror is tilted under an angle of $\alpha_{\max}/4$. Figure (4) shows this setup for one of the mirror pairs. The other one is assembled exactly the same but rotated 90° with respect to the first one, resulting in two dimensional collimation.

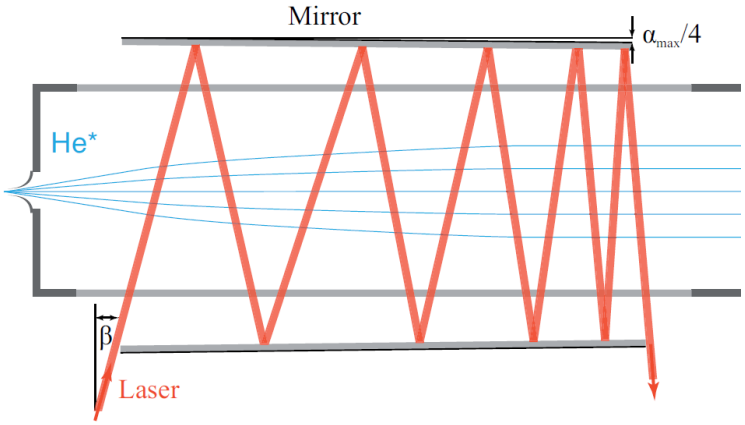

Figure 4: Sketch of the collimation scheme. 1083nm laser light enters the vacuum system directly after the skimmer under an angle β. Through reflection between two mirrors, each inclined by an angle of $\alpha_{\max}/4$, He* atoms are cooled in transversal direction resulting in a collimated atomic beam [25].

2.3 Zeeman Slower

Since a forward velocity of 800 m/s is far too high to capture the atoms in a trap, the collimated atomic beam has to be decelerated. For this, the atoms are slowed down by a resonant counter propagating laser beam: photons from this beam are absorbed and the atoms experience a recoil. The slowing down of the atoms leads to a change in the Doppler shift which causes the decelerated atoms to fall out of resonance with the laser light. In order to account for this problem, the commonly used technique of Zeeman slowing is applied. Here, a spatially varying magnetic field leads to Zeeman splitting of the atomic energy levels. The magnetic field can be tuned such that it compensates for the Doppler shift at every point of the Zeeman slower [28]. With this technique, the atoms are slowed down to less than 100 m/s.

2.4 Magneto-Optical Trap

The next steps towards a BEC are the spatial trapping of the atoms while increasing the density and decreasing the temperature. This is done with a magneto-optical trap (MOT). This kind of trap is commonly used in ultracold atom physics and is a crucial step towards Bose-Einstein condensation. The MOT provides a position dependent force field, whose center is located 20.5 cm behind the end of the Zeeman slower. This force field is created by combining a magnetic field with radiative forces of laser beams. Two coils in an anti-Helmholtz configuration generate the quadrupole magnetic field. Additionally, a homogeneous magnetic field in the center of the trap is supplied by three pairs of offset coils, which can be used to compensate

for static magnetic fields or slightly shift the center of the trap. Three pairs of counter-propagating laser beams, which are detuned by $-43\,\mathrm{MHz}$ from the atomic transition at 1083 nm, intersect in the center of the trap. In order to prevent interference with the laser light of the Zeeman slower, two of them are placed under 45° with respect to the direction of the decelerated beam (x-axis). Due to the circular polarization of the laser beams, σ^+ or σ^- transitions are induced. The MOT beams have a diameter of 3.6 cm and an intensity of $30 \times I_{\mathrm{sat}}$ per beam. The quadrupole magnetic field shifts the atomic energy levels such that doppler shifts are compensated for and the laser light is resonant with the atoms in the whole trap. The MOT-setup can be seen in Figure (5).

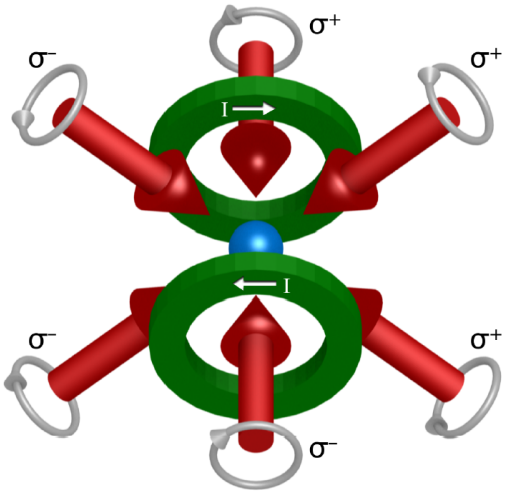

Figure 5: Three pairs of counter-propagating laser beams (red) and anti-Helmholtz coils (green) form the trapping potential for the magneto-optical trap (MOT). Arrows in the coils represent the direction of the current and gray arrows indicate the polarization of the laser light. The blue dot in the middle represents the atomic cloud trapped in the center [26].

With this setup, atoms can be cooled down to $\sim$ 1.5 mK and a cloud of about 10^9 atoms with radius of $\sim$ 1.2 mm can be achieved. The amount of atoms trapped in the MOT is limited by Penning ionization. This is a result of collisions of He* atoms with the hot background gas and between the trapped atoms themselves. In order to suppress the latter, the density in the MOT is kept low. Thus, further trapping steps have to be taken in order to achieve low temperatures and high enough densities for producing a BEC.

2.5 Magnetic Trap

As already mentioned, further cooling steps need to be done in order to create a BEC. This can be implemented with a magnetic trap. Atoms in the low-field seeking state $m = +1$ can be trapped in a magnetic field and at the same time losses due to Penning ionization can be avoided [29]. A so called cloverleaf trap, providing a non-zero minimum potential for trapping, is created in order to avoid Majorana spin flips. These spin flips occur at positions with vanishing magnetic field and would lead to severe trap losses [30]. For efficient transfer atoms from the MOT to the magnetic trap, the trap minimum is located at the center of the MOT.
As the trapping potential of the magnetic trap is not as deep as the one of the MOT, loading the atoms from the MOT into the magnetic trap is a sensitive process. To account for the shallower magnetic trap, during the decay of the MOT field, a 0.8 ms optical molasses pulse in three dimensions is applied, resulting in a further decrease of the cloud's temperature down to 1 mK. Directly after that, the currents for the cloverleaf trap are turned on. To capture as many atoms as possible, the size of the cloverleaf trap is at first approximately the size of the MOT and is downsized later. Since only atoms in the $m = +1$ state are trapped by the magnetic field, spin polarization of the atomic cloud is performed in order to transfer as many atoms as possible to the magnetic trap. This is done by using two counter-propagating σ^+ laser beams which are aligned along the quantization axis of the trap. These steps enable to transfer around 90% of the atoms into the magnetic trap. After that, with one dimensional laser cooling a temperature of ~ 120 μK is reached.
For further compression of the trap, the trap bottom is lowered to a minimum and the radial gradient as well as axial curvature are ramped up to their maximum values. This increases elastic collisions in the cloud, leading to further cooling and a higher phase-space density.
The last step in the magnetic trap is evaporative cooling [31]. Atoms are removed from the trap by inducing a spin-flip of the ones which have energies above a certain trap-depth value ϵ_t. This is done by radio-frequency (RF) induced evaporation. The remaining atoms rethermalize via elastic collisions until an equilibrium at lower temperatures is reached. The RF defines ϵ_t, therefore by lowering the frequency, ϵ_t can be subsequently lowered and the temperature decreased.

2.6 Optical Dipole Trap

As a last step towards Bose-Einstein condensation the atoms are loaded into a crossed optical dipole trap (ODT). In order to do this, the trap center of the magnetic trap and the center of the ODT overlap. The atoms in the ODT are cooled down to ~ 1 μK in the trap center.

In general, optical dipole traps offer trap depths below 1 mK and allow for trapping neutral atoms. The interaction of the induced electric dipole moment $p = \alpha E$ of the atom with the intensity $I(\vec{r})$ of the light field leads to a dipole potential:

$$U_{\mathrm{Dip}}(\vec{r}) = -\alpha \cdot I(\vec{r}) \ , \tag{2}$$

where α is the polarizability [32].
The dipole force $F_{\mathrm{Dip}}(\vec{r})$ then results in:

$$F_{Dip}(\vec{r}) = -\nabla U_{\mathrm{Dip}}(\vec{r}) \ . \tag{3}$$

In order to avoid heating processes like optical excitations in the trap, far red-detuned laser light was used for creating the trapping potential [33]. As found by Ashkin in 1978 [34], already a single gaussian laser beam can provide a trapping potential, as shown in Figure (6).

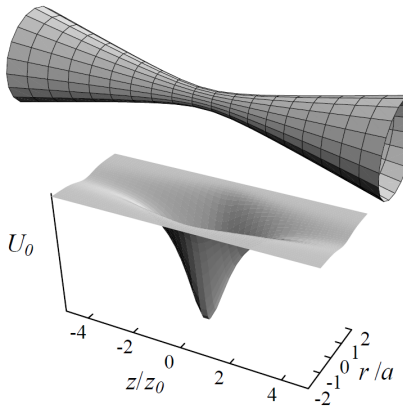

Figure 6: Optical dipole trap from a single gaussian laser beam. The upper part of the figure shows the focused beam along the z-axis and the lower part shows the resulting trapping potential along this axis [35].

Nevertheless, this potential is anistropic, offering weak confinement along the beam-propagation axis but tight confinement along the perpendicular directions. Thus, a crossed optical dipole trap, where two beams with orthogonal polarization overlay under 90°, can create a nearly isotropic 3D potential [32]. Such a trap is set up in the experiment with 2 perpendicular laser beams, both with wavelengths of 1550 nm and laser powers of ~ 4.5 W. Power control of the laser beams is done by acousto optical modulators (AOMs). For this, a 40 MHz sinusoidal RF signal is sent to the AOMs. The amplitude of this RF signal can be changed, in order to change the power in the trap beams.

2.7 Detection

Detection and investigation of the atomic cloud, which is produced with this experimental setup, is possible in two different ways: by using a delay-line detector (DLD) or through absorption imaging. While the first allows for single-atom detection, the latter allows for gathering information about size and density of the whole cloud and is in more detail explained in Chapter (3).

2.7.1 Delay Line Detector (DLD)

The delay-line detector is crucial for the experiment when it comes to single-atom detection. This is very important for quantum correlation and entanglement experiments as it enables 3D reconstruction of momentum space. The detector is mounted 80 cm below the trap center and consists of a micro-channel plate with delay lines beneath it on which read-out electronics are attached. A schematic drawing of the detector can be seen in Figure (7).

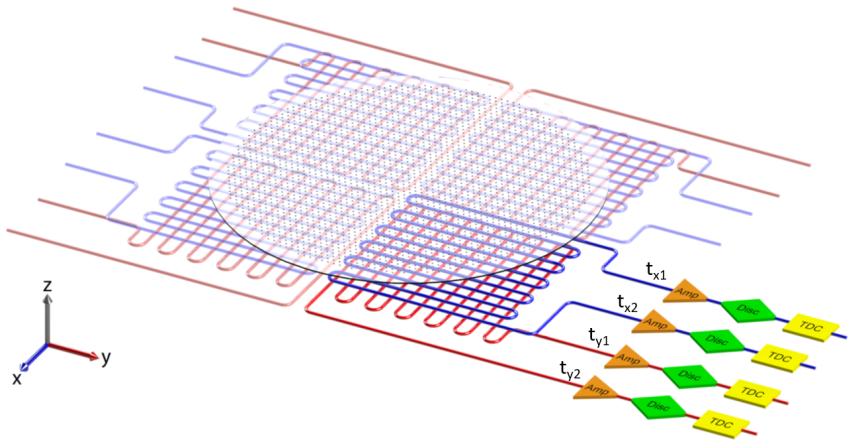

Figure 7: Delay line detector which is made out of four quadrants. Each of the quadrants consists of individual delay lines in x and y direction and seperate read-out electronics. A He* particle hitting the detector creates an electron avalanche which leads to an electric signal in the delay lines. This signal propagates along the wires, which go in x and y direction, to both ends respectively. At the end of the wires the four arrival times t_{x_1}, t_{x_2}, t_{y_1} and t_{y_2} are recorded [18].

Due to Penning ionization, an avalanche of electrons is created in the micro-channel plate when a He* atom hits the detector. Such an avalanche leads to electric pulses in each of the delay lines which propagate towards both ends of the delay line. The arrival times of these pulses allow the calculation

back to the position of the He* particle on the detector [18]:

$$\begin{aligned} x &\propto (t_{x_1} - t_{x_2}) \ , \\ y &\propto (t_{y_1} - t_{y_2}) \ , \end{aligned} \tag{4}$$

where t_{x_1} and t_{x_2} are the arrival times of an event – meaning the impact of an atom at the detector – at the two ends of the DLD in x direction, analogously for t_{y_1} and t_{y_2} in y direction. With this, a 3D image of momentum space can be reconstructed, as shown in Figure (8).

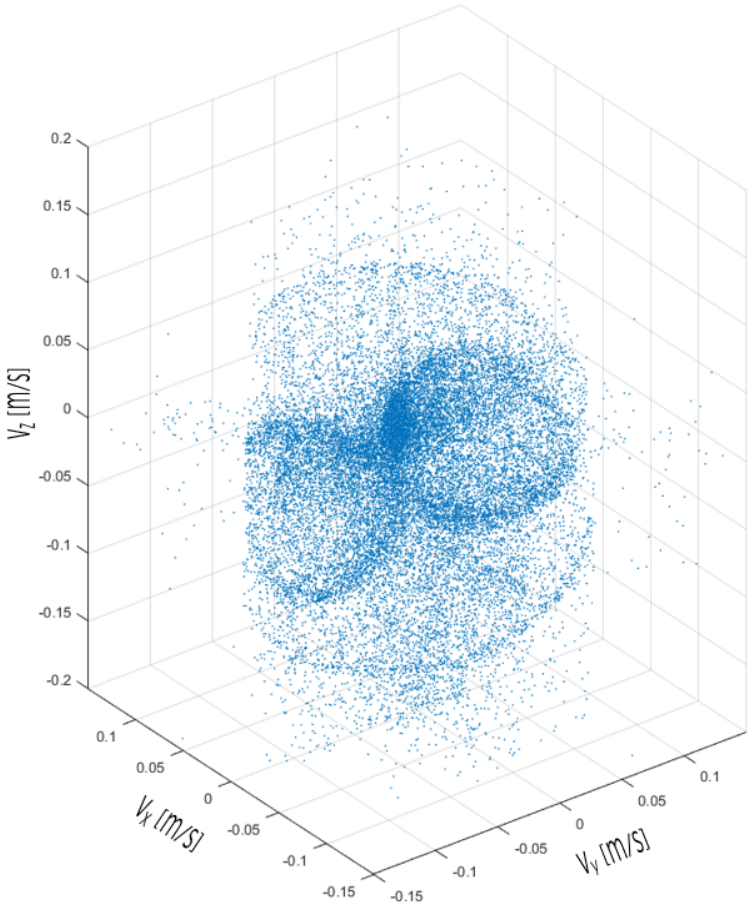

Figure 8: Reconstruction of the distribution of the atoms in 3D momentum space. Each dot represents the momentum of one single He* atom, measured with the delay-line detector.

Chapter 3 Absorption Imaging

The general idea of absorption imaging is the following: an absorptive medium with density $n(\vec{r})$ gets illuminated by a laser beam, the passed light is imaged via a camera, as shown in Figure (9).

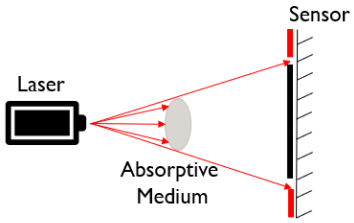

Figure 9: General concept of absorption imaging. An absorptive medium gets illuminated with resonant light, the resulting shadow is imaged via a camera/sensor.

Nevertheless, a couple of things have to be noted. The probe laser beam has to have its wavelength on or near to the atomic transition, such that absorption is possible. The intensity of the illuminating light should be kept below the saturation intensity of the atoms and has to be collimated.

3.1 Theoretical Description

According to Lambert-Beer's law, the intensity $I(\vec{r})$ of electromagnetic radiation propagating in x direction gets attenuated when passing through an absorptive medium with density $n(\vec{r})$ [26, 36]:

$$\frac{dI(\vec{r})}{dx} = -\sigma_a n(\vec{r}) I(\vec{r}) \ , \tag{5}$$

where σ_a is the scattering cross section.
In order to solve Equation (5), the method of separation of variables is used (it assumed that σ_a is constant within the whole atomic cloud):

$$\int_{I_{\text{in}}}^{I_{\text{out}}} \frac{1}{I} \, \mathrm{d}I = -\sigma_a \int_{-\infty}^{\infty} n(\vec{r}) \, \mathrm{d}x \ . \tag{6}$$

Solving this equation leads to:

$$\frac{I_{\text{out}}(y,z)}{I_{\text{in}}(y,z)} = e^{-\sigma_a \int_{-\infty}^{\infty} n(\vec{r}) \, \mathrm{d}x} \ . \tag{7}$$

3.2 Experimental Connection

Equation (7) emphasizes the relation between the intensities before and after the light being transmitted through the cloud. I_{out} is an absorption image I_{abs} taken after the light has propagated through the atomic cloud whereas I_{in} is given by an image taken without any atoms in the beam path, named I_{ref}. In order to minimize noise, a third image I_{bgr} with neither light nor atoms is taken and subtracted from both I_{abs} and I_{ref}. This leads to an expression for the transmission image $\frac{I_{\text{out}}(y,z)}{I_{\text{in}}(y,z)}$ which is accessible via absorption imaging technique in the experiment:

$$\frac{I_{\text{out}}(y,z)}{I_{\text{in}}(y,z)} = \frac{I_{\text{abs}}(y,z) - I_{\text{bgr}}(y,z)}{I_{\text{ref}}(y,z) - I_{\text{bgr}}(y,z)} \,. \tag{8}$$

In the interest of getting results for size, density and temperature of the cloud an expression for $n(\vec{r})$ has to be found for substituting it into Equation (7) such that the latter then can be fitted.

3.2.1 Fit Functions

For getting a functional expression for $n(\vec{r})$ the two possible states of the atomic cloud have to be taken into account: a thermal cloud and a BEC (or rather a mixture of both cases, meaning some atoms are already condensed into a BEC and some are still in a thermal state).

Thermal cloud
The thermal cloud has a Gaussian shape with central position (x_0, y_0, z_0)[37]:

$$n(\vec{r}) = n_0 \prod_{i \in \{x,y,z\}} exp\Big(- \frac{(i - i_0)^2}{2\sigma_i^2} \Big) \,, \tag{9}$$

where n_0 is the central density of the cloud, i_0 define the center of the cloud and σ_i are the radii of the cloud.
For a freely falling cloud in z-direction, σ_z evolves in time t according to:

$$\sigma_z(t) = \sqrt{\frac{k_B T}{m} t^2 + \sigma_z^2(0)} \,, \tag{10}$$

where $\sigma_z(0) = \frac{k_B T}{m\omega_z^2}$, with Boltzmann's constant k_B, temperature T of the cloud and mass m [38] p.27. A complete derivation of Equation (10) can be found in Appendix (A.1).
By using Equation (9), the total number of atoms in the cloud is given by:

$$N = \int_V n(\vec{r}) \, \mathrm{d}V = n_0 (2\pi)^{3/2} \sigma_x \sigma_y \sigma_z \,. \tag{11}$$

With this expression for the atom number N, it is possible to express σ_x in terms of N and arrive at:

$$\begin{aligned}\int_{-\infty}^{\infty} n(\vec{r})\,\mathrm{d}x &= n_0\sigma_x\sqrt{2\pi}\,\exp\Big(-\frac{(y-y_0)^2}{2\sigma_y^2}\Big)\exp\Big(-\frac{(z-z_0)^2}{2\sigma_z^2}\Big)\\ &= \frac{N}{2\pi\sigma_y\sigma_z}\exp\Big(-\frac{(y-y_0)^2}{2\sigma_y^2}\Big)\exp\Big(-\frac{(z-z_0)^2}{2\sigma_z^2}\Big)\,.\end{aligned} \tag{12}$$

By combining Equations (7) and (12) one ends up with:

$$\frac{I_{\mathrm{out}}(y,z)}{I_{\mathrm{in}}(y,z)} = \exp\left(-\sigma_a\frac{N}{2\pi\sigma_y\sigma_z}\exp\Big(-\frac{(y-y_0)^2}{2\sigma_y^2}\Big)\exp\Big(-\frac{(z-z_0)^2}{2\sigma_z^2}\Big)\right). \tag{13}$$

In the case of a thermal cloud, this function is finally fitted to the transmission image with the five fit parameters y_0, z_0, σ_y, σ_z and N.

BEC

Below the critical temperature T_c the ground state density distribution for the condensate can be found by solving the Gross-Pitaevski equation in the mean-field formalism [39]:

$$i\hbar\frac{\partial}{\partial t}\Phi(\vec{r},t) = \Big(-\frac{\hbar^2\nabla^2}{2m} + U_{\mathrm{ext}}(\vec{r}) + g|\Phi(\vec{r},t)|^2\Big)\Phi(\vec{r},t)\,, \tag{14}$$

where the coupling constant g is related to the scattering length a via $g = \frac{4\pi\hbar^2 a}{m}$ and U_{ext} is an external potential (trapping potential). The ground state for noninteracting bosons can be obtained by using the following product ansatz for the condensate wave function:

$$\Phi(\vec{r},t) = \Phi(\vec{r})e^{-\frac{i\mu t}{\hbar}}\,, \tag{15}$$

with the normalization condition $\int \mathrm{d}\vec{r}\ \Phi^2(\vec{r}) = N$, where N is the total number of particles and μ being the chemical potential of the condensate. With this ansatz, Equation (14) becomes:

$$\mu\Phi(\vec{r}) = \Big(-\frac{\hbar^2\nabla^2}{2m} + U_{\mathrm{ext}}(\vec{r}) + g|\Phi(\vec{r})|^2\Big)\Phi(\vec{r})\,. \tag{16}$$

This can be further simplified by using the Thomas-Fermi approximation [38] (p.168), which neglects the kinetic term in Equation (16):

$$\mu\Phi(\vec{r}) = \big(U_{\mathrm{ext}}(\vec{r}) + g|\Phi(\vec{r})|^2\big)\Phi(\vec{r})\,. \tag{17}$$

With the solution:

$$n_{\mathrm{BEC}}(\vec{r}) = |\Phi(\vec{r})|^2 = \frac{1}{g}\big(\mu - U_{\mathrm{ext}}(\vec{r})\big)\ . \tag{18}$$

According to Kotyrba [26], the density profile of the condensate in a harmonic trap has a parabolic shape:

$$n_{\mathrm{BEC}}(\vec{r}) = \frac{15N_c}{8\pi r_x r_y r_z}\max\Big\{0,\ \ 1-\big(\frac{x}{r_x}\big)^2-\big(\frac{y}{r_y}\big)^2-\big(\frac{z}{r_z}\big)^2\Big\}\ . \tag{19}$$

After integrating, one ends up with:

$$n_{\mathrm{BEC}}(y,z) = \int_{-\infty}^{\infty}\mathrm{d}x\ n_{\mathrm{BEC}}(\vec{r}) = \frac{15N_c}{2\pi r_y r_z}\mathrm{Re}\Big\{\Big(1-\big(\frac{y}{r_y}\big)^2-\big(\frac{z}{r_z}\big)^2\Big)^{3/2}\Big\}\ , \tag{20}$$

leading to the following fit function in case of a BEC:

$$\frac{I_{\mathrm{out}}(y,z)}{I_{\mathrm{in}}(y,z)} = \exp\left[-d_{\mathrm{BEC}}\,\mathrm{Re}\Big\{\Big(1-\big(\frac{y}{r_y}\big)^2-\big(\frac{z}{r_z}\big)^2\Big)^{3/2}\Big\}\right]\ , \tag{21}$$

with $d_{\mathrm{BEC}} = \frac{15N_c\sigma_a}{2\pi r_y r_z}$. In this case r_y, r_z and d_{BEC} are the fit parameters.

3.3 Previous Experimental Imaging Setup

For absorption imaging, resonant laser light at 1083 nm is used with an intensity of $0.01 \times I_{\mathrm{sat}} \approx 2\,\mu\mathrm{W/cm^2}$. The setup of the absorption imaging system can be seen in Figure (10). The atomic cloud is trapped in the center of the main vacuum chamber, either in the magnetic trap, the MOT or the dipole trap, before being released for some time of flight. The imaging light enters the chamber under an angle of 22.5° with respect to the x-y-plane. Previously, an EMCCD[7] camera has been used to image the atomic cloud. The imaging system was designed to demagnify the image by a factor of 4, resulting in one pixel corresponding to approximately $32\,\mu$m in the object plane. These facts led to a few unintended problems:

1. At 1083 nm the EMCCD camera shows a quantum efficiency of less than 1%. As it is known how many photons are typically impinging on the sensor, the small quantum efficiency would lead to an average registration of 10 photons per pixel[8]. This fact led so far to a noisy final image when dividing two images by each other (shown in Figure (11)).

[7] electron-multiplying charge coupled device

[8] Using higher intensity for illuminating the cloud is not possible, as that would already exceed the saturation intensity of the atoms.

2. The demagnification of the imaging system resulted in a rather coarse grained image and set a limit to the resolution of the system.

3. As the imaging light does not illuminate the released cloud perpendicular to its direction of free fall (z-axis), unintended effects such as distortion or small depth of field played an even bigger role.

Therefore, the goal of this thesis was to investigate alternatives to the previously used imaging system and ideally implement a new one, either instead or in addition to the one used so far. In order to do so, another type of camera was considered – an InGaAs-camera, made with indium gallium arsenide. This material is a semiconductor with a band gap of 0.750 eV at room temperature [40], which corresponds to the energy of photons with a wavelength of $\sim$ 1653 nm. It has been found that a photo-detector made out of this material allows detection of photons in the infrared regime with a significantly better quantum efficiency than EMCCD cameras. Thus, several companies offering InGaAs-cameras were contacted and information was gathered. After comparing the different offers, a few of the companies were requested to first provide a test-model.
For improving the imaging system, it was not only decided to exchange the EMCCD camera but also to improve on the imaging lens. The current magnification of 1/4 is a limiting factor for the resolution of the system, therefore it was decided to design a lens-system which actually magnifies the

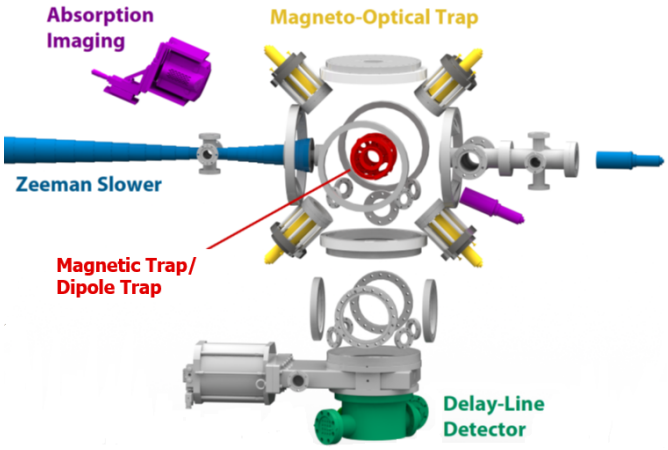

Figure 10: Absorption imaging setup (violet) at the main vacuum chamber. The atomic cloud gets illuminated with an intensity of $\sim 2\,\mu\mathrm{W/cm^2}$ of 1083 nm light after being released from a trap. The illuminating light enters the main vacuum chamber under an angle of 22.5° with respect to the x-y-plane. The shadow of the freely falling cloud is imaged with an EMCCD camera.

atomic cloud. The fact that the atomic cloud expands under free fall after being released from the trap sets a maximum limit on the magnification M, since the cloud should still be visible after a few milliseconds of time of flight. This maximum limit was calculated to be $M \approx 2.8$. Thus, the lens-system was designed in a way such that it magnifies the cloud by a factor of ~ 2.

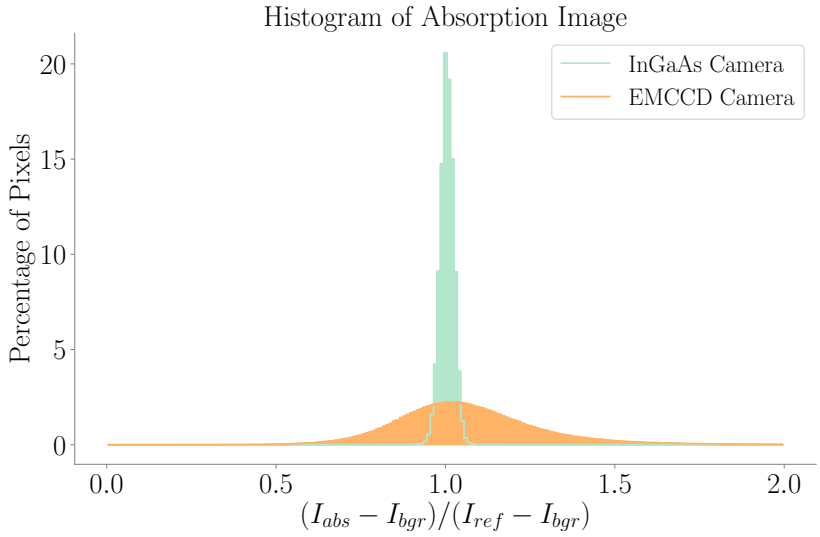

Figure 11: Histograms of absorption images taken with the previously installed EMCCD camera and with an InGaAs camera. The absorption image is the result of the division of images, as shown by Equation (8). The width of the EMCCD-histogram already suggests that images taken with that camera are quite noisy. This results from the low quantum efficiency in the infrared region. The InGaAs camera clearly leads to a much narrower histogram (it results from the division of two images taken with one of the test cameras, the Cheetah 400Hz). This indicates that the InGaAs cameras could lead to a significant improvement concerning noise in the images.

3.4 Testing InGaAs Cameras

After comparing the properties of different InGaAs-cameras, it was decided to request the following camera models for the first test:

- **Widy SWIR** from New Imaging Technologies (NIT)[9]
- **Ninox** from Raptor Photonics[10]
- **Cheetah 400Hz** from Xenics[11]
- **Bobcat** from Xenics

In order to investigate which camera model would improve the imaging system best, several tests were done:

1. Comparing dark noise and read noise depending on temperature and exposure time of the camera.
2. Verifying the analog to digital (A/D) conversion stated in the respective data sheets.
3. Investigating how the performance of the camera depends on the illumination, if the other two tests were promising.

In order to perform these tests, a linear ND filter, a grid distortion target and a resolution target (all from Thorlabs) were used.

3.4.1 Dark Measurements

As one of the main goals of the new imaging system is decreasing the noise level, it is important to test the camera models' dark and read noise levels. Dark noise results from thermal photons which produce an electric signal in the sensor – this noise source is sometimes referred to as thermal noise – whereas read noise arises from electric noise of the on-chip amplifier and other electronic components. For testing this noise levels, dark measurements (no illumination at all) at different exposure times were done with all four test models. Especially interesting for the application of the camera in the experimental setup are short exposure times in the range of 30 to 50 μs. All measurements were done in the high gain mode setting, as low gain mode was supposed to be not sufficient for the low light-intensities used in the experiment. Further, an effort was made to test the four cameras at the same temperature, which was possible for all expect the Widy (the

[9] New Imaging Technologies (NIT): 1 impasse de la Noisette, Bat D, 1er étage; 91370 Verrières le Buisson - France.

[10] Raptor Photonics Limited: Willowbank Business Park, Larne, Co. Antrim, BT40 2SF, Northern Ireland.

[11] Xenics nv: Ambachtenlaan 44, BE-3001 Leuven, Belgium.

camera stabilized around 30°C instead of 25°C). When analyzing such dark measurements with longer exposure times, a linear increase in the noise can be expected. The offset at the y-axis corresponds to read noise whereas the slope corresponds to dark noise. The measured noise profiles for the four test cameras can be seen in Figure (12). It is visible that only one of the four cameras exhibits the expected linear behavior, namely the Cheetah 400Hz camera. In order to explain the data obtained with the Ninox camera, further tests were done with different software settings. After that, it was realized that the Ninox camera only offers exposure times longer than 100 μs in the high gain mode. Therefore, the dark measurements at short exposure times in high gain mode are not meaningful as it is unclear what the camera did at this settings. The unexpected decrease in dark-behavior of the Widy camera has so far not been explained.

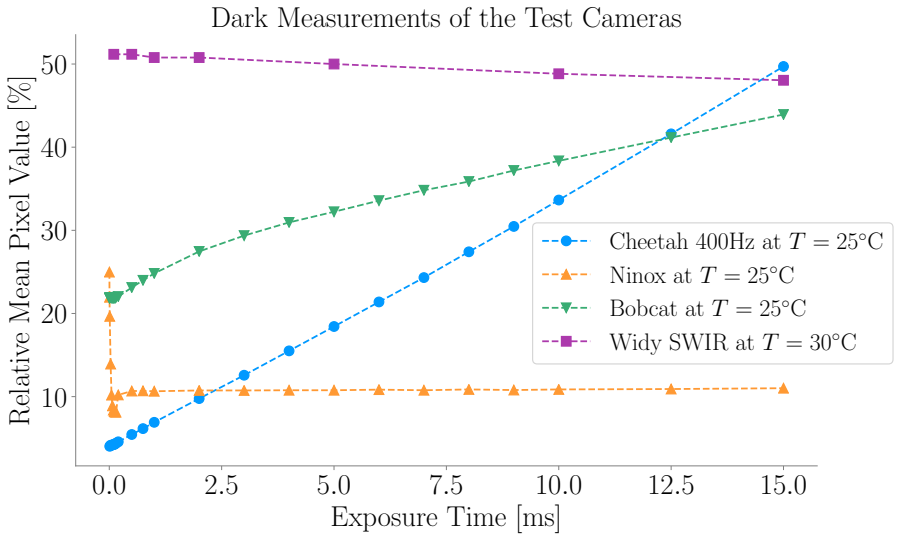

Figure 12: Dark Measurements of the four test cameras for different exposure times at constant temperature settings and in high gain mode. The Cheetah 400Hz camera is the only one showing the expected linear behavior. The noise profile of the Ninox is explained by the fact that this camera only offers exposure times above 100 μs in high gain mode. The decreasing behavior of the Widy SWIR is so far not explained. For very short exposure times of less than 1 ms, the Bobcat shows a significantly higher noise profile than the Cheetah 400Hz.

3.4.2 Analog to Digital (A/D) Conversion

The A/D conversion of the camera is the second important quantity as this value corresponds to a resolution of intensity. The more bit values are available for each pixel the higher the contrast between noise and the actual light-signal can be. Thus, a higher A/D conversion value corresponds to a higher dynamic range of the camera, leading to a higher signal to noise ratio. In order to verify the A/D values listed in the datasheets, a dark and a saturated image taken with each respective camera were analyzed and results are represented in the respective histogram, seen in Figure (13). In the datasheets of all four cameras an A/D conversion of 14 bits was listed. Nevertheless, the histograms show that none of these cameras actually offer $2^{14} = 16384$ different pixel values. With the software of the Widy camera, it was only possible to save 8 bit images, resulting in an A/D conversion of 8 bits ($2^8 = 256$). The Bobcat camera shows offsets from the minimum and maximum, resulting in a value between 12 and 14 bits A/D. The Ninox camera as well as the Cheetah 400Hz only provide $2^{12} = 4096$ different pixel values. Nevertheless, the Cheetah 400Hz is the only camera model accessing the full range of 4096 pixel values without any offsets at the edges .

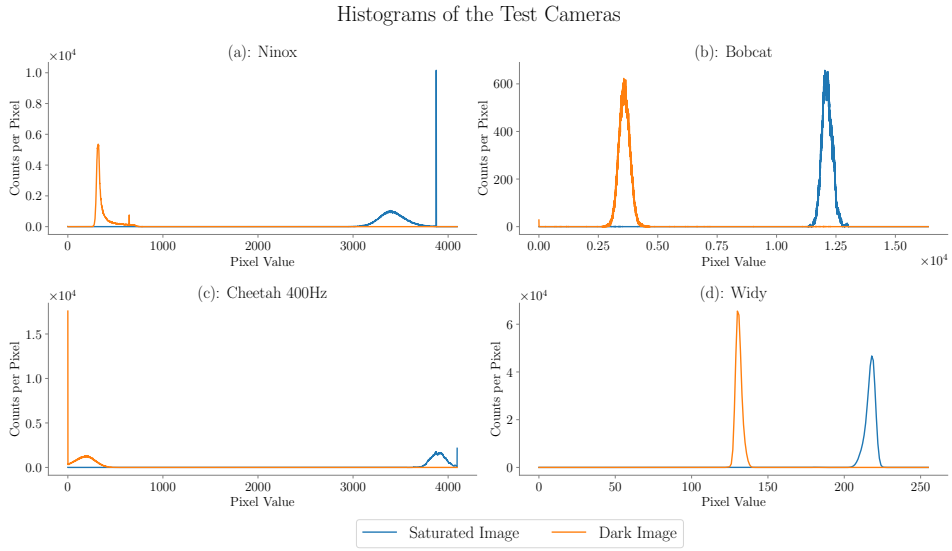

Figure 13: Histogram of dark and saturated images taken with the respective test cameras. According to the data sheets, all four camera models should offer 14 bits analog to digital conversion, corresponding to $2^{14} = 16384$ different accessible pixel values. The histograms show that none of them actually do. The Widy shows 8, the Ninox and the Cheetah 400Hz 12 bits and the Bobcat shows a value between 12 and 14 bits. Offsets from zero and maximum value are visible in all histograms except for the Cheetah 400Hz camera.

3.5 Cheetah 400Hz and Cheetah 110Hz

Despite some deviations from the datasheet (A/D conversion), the Cheetah 400Hz camera performed best during the previously described measurements. It showed a linearly increasing dark noise behavior and offered at least a 12 bit A/D conversion. Thus, with this camera a third test was done, concerning the illumination dependent performance. A linear ND-filter from Thorlabs was placed in the test setup during constant laser intensity. This offered the possibility to investigate if the performance of the camera does linearly depend on the illumination of the sensor. Figure (14) shows the expected linear behavior.

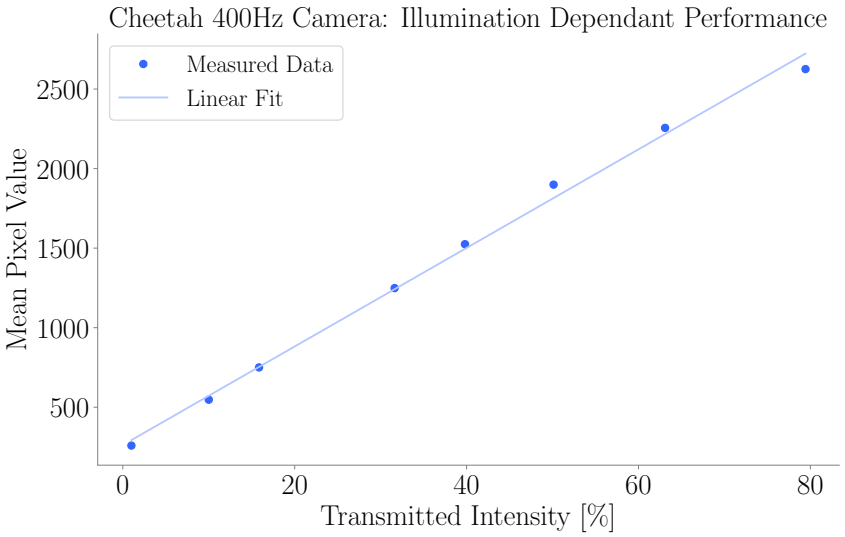

Figure 14: Images taken at constant laser intensity with the linear ND filter placed in front of the Cheetah 400Hz camera. The offset can be explained by dark and read noise: even if no light is hitting the sensor, a signal results from these two noise components.

Additionally, it was decided to also investigate shot noise in the images which results from the quantum efficiency of the respective camera model. Therefore, an object was placed in front of the camera and 50 images where taken directly after each other without neither changing the conditions nor the software settings. Subsequently dividing each image out of the fifty test images by each one to get better statistics leads to a mean pixel value $\bar{p}$ and a standard deviation σ for a divided image of:

$$\bar{p} = 1.003 \, , \sigma = 0.012 \, . \tag{22}$$

The comparison with the previous EMCCD camera is shown in Figure (11), revealing that the histogram of an image resulting from the division of two images taken with the EMCCD camera is much more broad than the one taken with the Cheetah 400Hz camera. This suggests that the higher quantum efficiency of the Cheetah 400Hz camera leads to a much better imaging performance and less shot noise in the final images.

Finally, after consulting the technical support from Xenics, it was decided to purchase the Cheetah 110Hz model. This model offers 110 Hz frame rate instead of 400 Hz and should - according to the technical support - exhibit 14 bit A/D conversion. In order to ensure that the newly ordered Cheetah 110Hz camera model works according to the data sheet, test measurements were repeated before implementing the camera in the experimental system. Dark measurements were done in high gain mode at different exposure times and also at two temperature settings as this camera model offers low sensor temperatures due to a water-cooled TE3[12] element. Figure (15) shows the expected noise behavior.

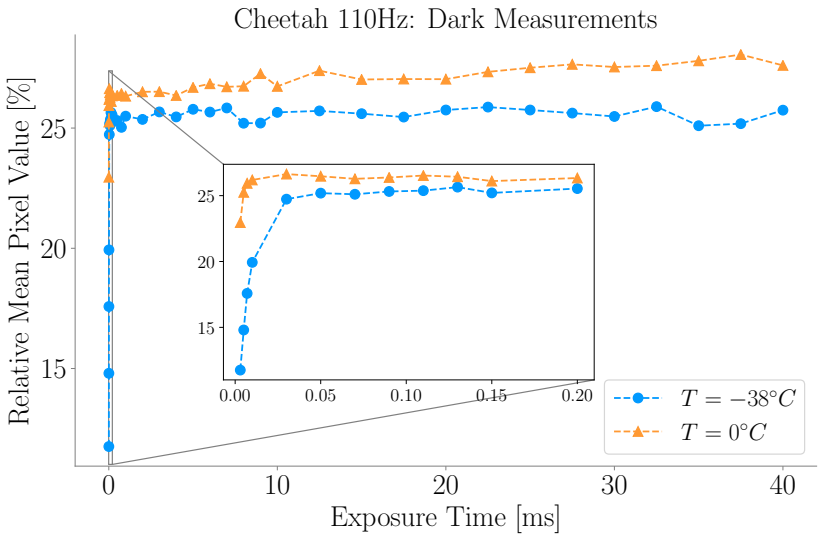

Figure 15: Dark measurements done with the Cheetah 110Hz camera in High Gain mode for different exposure times and two temperature settings. Dark noise is almost constant at very low temperatures of $T = -38°C$ and also at a lower level compared to the temperature setting of $T = 0°C$.

[12]Three-stage Peltier cooler.

3.6 Changes on the Imaging System: The M ≈ 2 Lens

In order to test the camera models under experimental conditions, a test setup was designed. In order to achieve the desired magnification of 2, an imaging system consisting of two lenses was built. An important restriction on the system is given by the main vacuum chamber (see Figure (10)) in which the atoms are trapped. The distance from the trap center to the flange through which the cloud is imaged is 275 mm. Therefore the minimum object distance g_1 for the first lens of the imaging system was set to 275 mm. Hence, a plano-convex AR-coated lens with focal length $f_1 = 200$ mm was used as a first lens and placed 400 mm behind the test object. In a distance of 400 mm after this lens, an equally sized image is created. As space at the experimental system is limited, the second lens was chosen with a small focal length of $f_2 = 24.5$ mm was chosen. In order to receive the desired magnification, calculations were done to find the correct distance for the second lens. The magnification M of this two-lens imaging system can be calculated according to:

$$M = M_1 \cdot M_2 = \frac{b_1}{g_1} \cdot \frac{b_2}{g_2} \,, \tag{23}$$

with b_i and g_i being the image distance and the distance to the object of the respective lenses. By using the lens equation:

$$\frac{1}{f} = \frac{1}{b} + \frac{1}{g} \,, \tag{24}$$

or

$$b = \frac{f \cdot g}{g - f} \,, \tag{25}$$

the magnification (Equation (23)) can be expressed in terms of focal lengths and object distances:

$$M = \frac{\frac{f_1 \cdot g_1}{g_1 - f_1}}{g_1} \cdot \frac{\frac{f_2 \cdot g_2}{g_2 - f_2}}{g_2} = \frac{f_1 \cdot g_1}{g_1(g_1 - f_1)} \cdot \frac{f_2 \cdot g_2}{g_2(g_2 - f_2)} = \frac{f_1}{(g_1 - f_1)} \cdot \frac{f_2}{(g_2 - f_2)} \,. \tag{26}$$

From this, one can find an expression for the object distance g_2 required for a favorable magnification M:

$$g_2 = \frac{f_1 \cdot f_2}{M(g_1 - f_1)} + f_2 \,, \tag{27}$$

leading to an object distance of $g_2 = 38.1\,\text{mm}$ for $M = 2$ in the case of $g_1 = 400\,\text{mm}$, $f_1 = 200\,\text{mm}$ and $f_2 = 24.5\,\text{mm}$. With Equation (25) and

the values for g_2 and f_2, the image distance after the second lens can be calculated to $b_2 = 68.6$ mm. From Equation (27), it can be seen that smaller magnifications can be reached by increasing the object distance g_2.
For the test setup, a 1083 nm laser is used as a light source. This is followed by a fiber coupler to collimate and expand the beam. Then a translation stage, where a test object can be mounted, is placed. After that, a mount for a powermeter is placed in order to have the possibility to measure the power of the laser beam. This is followed by a vacuum chamber window to simulate the conditions from the experiment.The first lens with focal length f_1 of 200 mm is placed 400 mm after the object. At a distance of 438.1 mm after this, a second lens with focal length f_2 of 25.4 mm is mounted. The camera is placed such that the magnified image arising 68.6 mm after the lens is imaged on the sensor. In front of the camera, a bandpass filter for 1083 nm is placed (to ensure that only laser light hits the sensor). An iris is placed in the focus point between camera and second lens. The whole test setup can be seen in Figure (16) and was used for the test measurements which are described in Chapter (3.7).

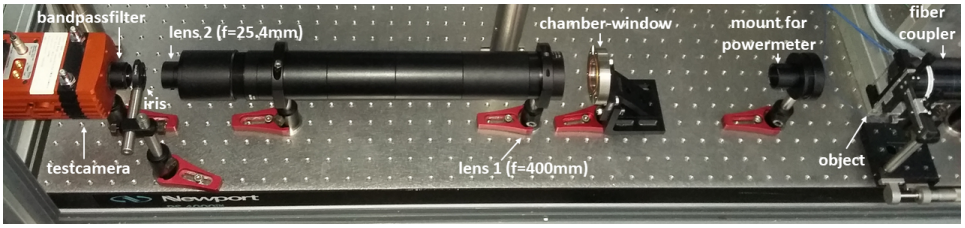

Figure 16: For testing the different InGaAs-cameras, a 1083 nm laser beam is collimated and enlarged with a fiber coupler, followed by a mount for placing different test objects. After that, a mount for a power meter is placed in order to enable measuring the power of the laser beam. Further, a vacuum-chamber window is placed to simulate the conditions of the experiment. The first lens with $f_1 = 200$ mm is mounted 400 mm after the object, resulting in a one to one image 400 mm behind the lens. This image acts as an object for the second lens with $f_2 = 25.4$ mm which is placed 38.1 mm behind this virtual object. This results in a sharp image 68.6 mm after the second lens, which is magnified by ~ 2. In front of the camera, an iris is placed at the focus point and a bandpass filter is mounted directly onto the camera.

3.7 Previous Imaging System in Comparison to the Newly Designed System

In this chapter, not only the previously installed EMCCD camera and the new Cheetah 110Hz camera are compared but also the imaging lens will be investigated and analyzed.

3.7.1 Comparison Between the Old EMCCD and the New InGaAs Camera

Even though the for this experiment most important difference between these two cameras is their respective quantum efficiency, also other properties like dark behavior and A/D conversion were compared. The previously installed EMCCD camera from Andor[13] offers according to the data sheet a quantum efficiency of less than 1 % in the infrared region whereas the newly purchased InGaAs camera Cheetah 110Hz from Xenics offers according to the datasheet (see Appendix (A.2)) $\sim$ 70% quantum efficiency at the wavelenght used in the experiment.
Dark measurements were done with both cameras at approximately the same temperature for different exposure times. Figure (17) shows the results. The EMCCD camera from Andor has dark noise less than 3%. The Cheetah 110Hz shows linearly increasing dark behavior for very short exposure times followed by a constant noise level of $\sim$ 25%.

[13] Andor, 277.3 mi, Belfast, UK.

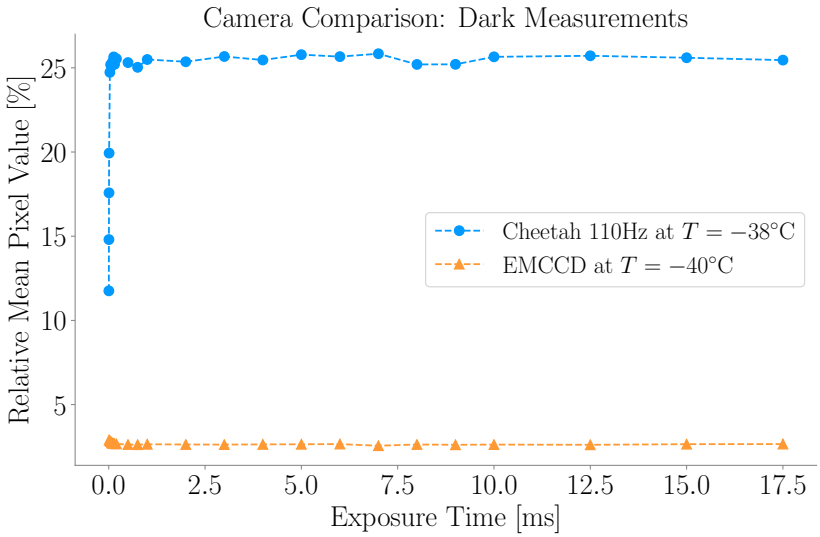

Figure 17: Dark measurements for different exposure times done with the old EMCCD camera at $T = -40°C$ and the new Cheetah 110Hz camera at $T = -38°C$ are shown. The dark noise of the EMCCD is less than 3% and therefore negligible. For the Cheetah 110Hz, dark noise increases at short exposure times and settles to a constant level of $\sim 25\%$.

The histograms in Figure (18) of a dark and a saturated image taken with the old EMCCD camera and the new InGaAs camera respectively show that both cameras use their dynamic range until the upper end which corresponds to $2^{14} = 16384$ different pixel values. When comparing the lower ends of the histograms (18a) and (18b) it is visible that the histogram of the dark image taken with the Cheetah 110Hz camera is shifted to higher pixel values. This effect is due to the dark noise of this camera: The histogram is shifted to pixel values of ~ 5000, which is about 30% of the maximum possible value of 16384. This is consistent with previously presented results of the dark measurements (see Figure (17)).

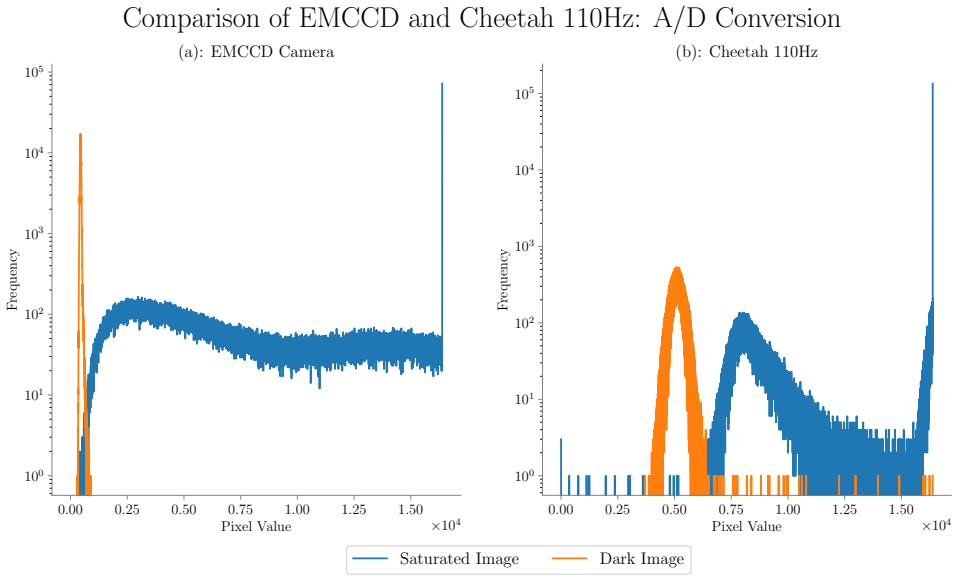

Figure 18: Comparison of the dynamic ranges of the EMCCD and the new InGaAs camera. For this, one dark and one saturated image were taken at room temperature with the respective camera. Both cameras saturate at a pixel value of $2^{14} = 16384$. The dark image taken with the Cheetah 110Hz in Figure (b) is shifted to pixel values of ~ 5000, which is about 30% of the maximum possible value of 16384 and thus consistent with the dark noise (see Figure (17)).

3.7.2 Comparisons between the Old M $\approx 1/4$, the Selfmade M $\approx$ 2 and the Telecentric M=0.28 Lenses

During the camera tests, the newly designed imaging lens-system was investigated and tested. In the course of this, one problem of the imaging system became clear. The effect of using two standard plano-convex lenses (and one of them with a focal length of 25.4 mm and therefore a quite large curvature) leads to pincushion distortion in the images. This unintended effect can be seen in Figure (19) and leads problems when it comes to analyzing the images. As one can see below, the magnification increases at the edges of the field of view which is a problem for getting information about the size of the atomic cloud. With such a distorted image, the size of the atomic cloud can only be determined properly when the cloud is in the middle of the image but not at the edge.

Thus, adapting and improving the imaging system was attempted. Here it has to be said that it is in general possible to determine the distortion effects directly at the experiment and then account for them when evaluating the absorption images. For the BEC experiment, this would comprise opening

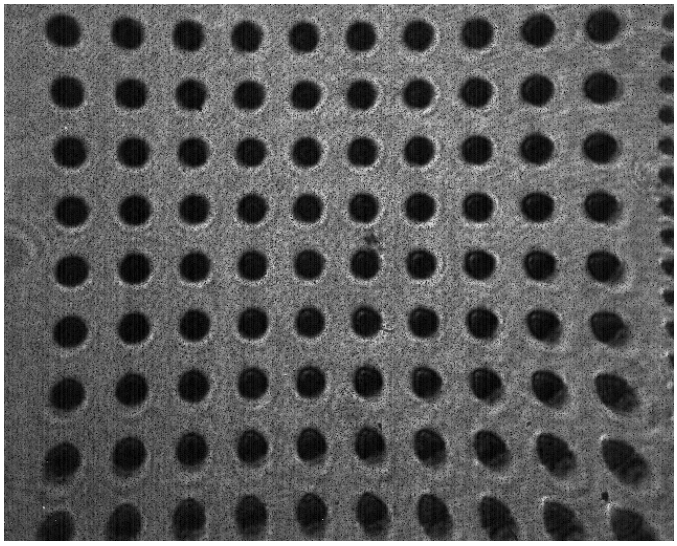

Figure 19: Distortion effects of the two-lens imaging system with magnification $M \approx 2$. The image was taken with the Cheetah 110Hz camera.

the main vacuum chamber in order to placa a distortion grid at the place where normally the BEC is produced. In order to avoid contamination of the vacuum system, it was decided to replace the two separate lenses with focal lengths f_1 and f_2 with a so called telecentric lens. A telecentric lens system is by definition a system, in which the chief rays on the image side are parallel to the optical axis and thus perpendicular to the image plane [41]. This leads to the fact, that the magnification is independent of the distance of the object. It can be placed anywhere within the depth of field [42]. The basic idea to realize such a telecentric system is the placement of a pinhole in the focal plane between two lenses. With that, only collimated rays reach the image plane. The field of view of such a system is limited to the aperture of the objective lens [43].
Two telecentric lenses were purchased[14] - one with a magnification of 0.28 and one with a magnification of 1.85. The latter one unfortunately has a lead time of 5 months in total and thus can not be investigated within this Master Thesis. Nevertheless, the distortion effects for the other three different objectives can be seen in Figure (20). A distortion grid was imaged with the new Cheetah 110Hz camera in all three cases. The telecentric lens in Figure (20a) shows no obvious distortion effects and is therefore a huge improvement compared to the old objective, which showed surprisingly strong pincushion distortion (see (20b)). Figure (20c) shows again the distortion effects of the self built $M \approx 2$ objective (placed here again for better comparison).

[14] Sill Optics GmbH und Co. KG, Johann-Höllfritsch-Str. 13, 90530 Wendelstein, Germany.

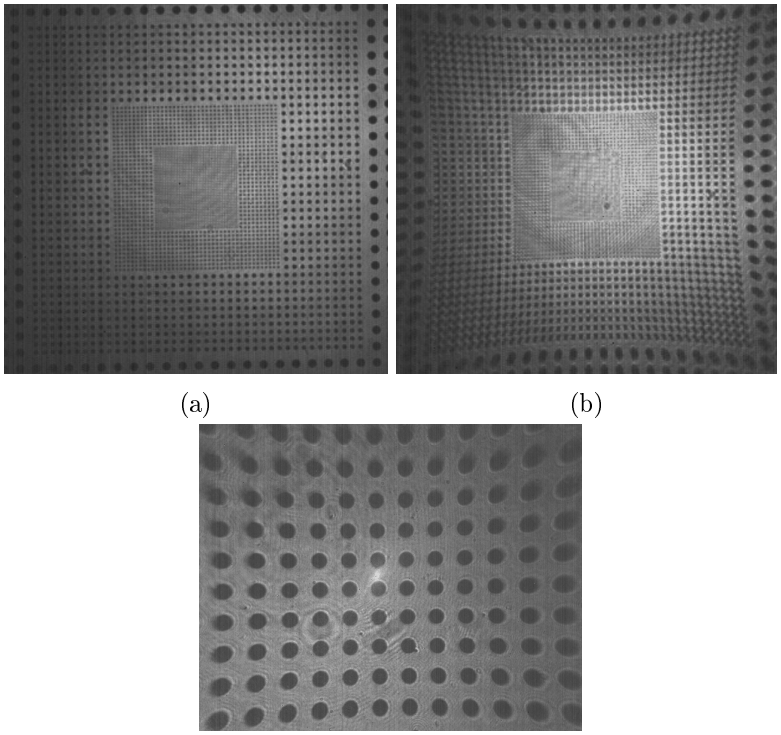

(a) (b)

(c)

Figure 20: Investigation of distortion effects for the different objectives. All images were taken with the Cheetah 110Hz camera. Figure (20a) shows a grid distortion target imaged with the telecentric lens, no distortion effects are visible. Figure (20b) was imaged with the old objective, clearly showing distortion effects as well as Figure (20c), which was imaged with the selfmade $M \approx 2$ objective.

The resolution of the imaging system consists of the resolutions of the camera and the objective. In Figure (21), the images taken for testing the resolution of the different lenses can be seen. All three images were taken with the new Cheetah 110Hz camera. It can be seen, that the telecentric lens in Figure (21a) shows better resolution than the old $M \approx 1/4$ objective in Figure (21b). When looking at the self made $M \approx 2$ objective in Figure (21c), its higher magnification needs to be taken into account. Therefore, it is not directly comparable with the other two objectives. However, it can be concluded that compared to a standard lens system, a telecentric lens with the same magnification offers the better resolution.

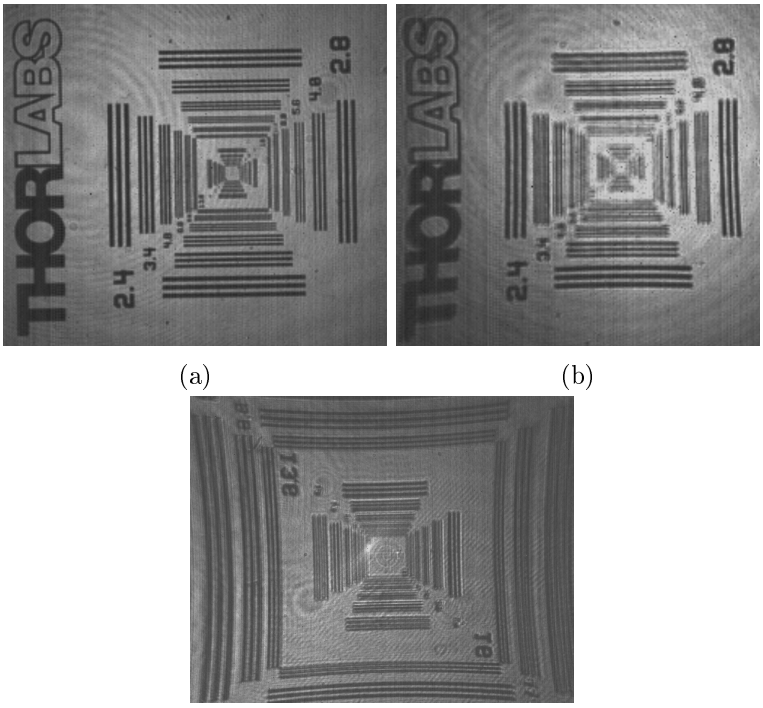

(a) (b)

(c)

Figure 21: All images for the resolution tests were done with the Cheetah 110Hz camera. Figure (21a) shows an image taken with the new telecentric lens. Figure (21b) was taken with the old M $\approx 1/4$ lens and Figure (21c) was taken with the selfmade M ≈ 2 lens. Even without further detailed analysis it is obvious that the telecentric lens offers the highest resolution.

For the new imaging system with the telecentric lens, the camera's pixel size of $20\,\mu$m together with the magnification $M = 0.28$ of the objective leads to one pixel corresponding to $70\,\mu$m in the object plane. The simulated resolution of the telecentric lens is shown in Figure (22). At the experiment, the field of view is limited by the window of the vacuum chamber. This leads to the fact that all the light, which is registered by the sensor, impinged on the lens within a circle of $r = 17.5\,$mm. Thus, the solid red (21.75 mm tangential) and the solid green (27.5 mm tangential) curves can be excluded for the discussion of resolution at the system. An idea of the least resolution can be gained by analyzing the blue (0.0 mm tangential) curve. Under the assumption that a value of 0.5 for the modulus of the OFT (optical transfer function) still leads to a high enough contrast, about 12.5 cycles per mm can be resolved. Thus, the least resolution of the telecentric lens at the experiment is $1/(2 \cdot 12.5) = 40\,\mu$m. Therefore, the resolution of the imaging system is limited by the pixel size of the camera.

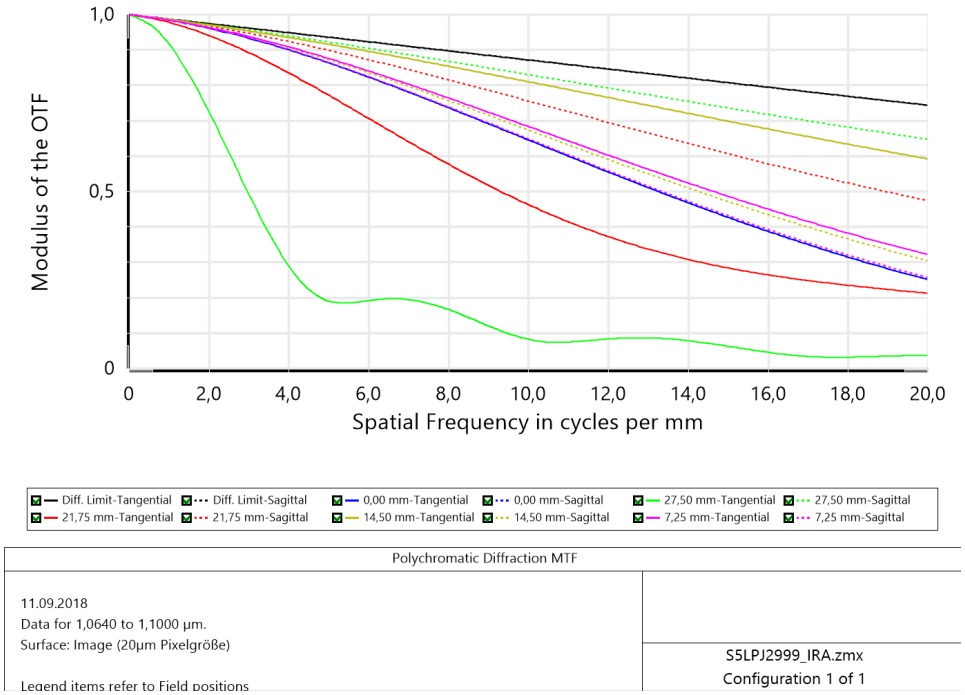

Figure 22: Simulated resolution of the telecentric lens. For an estimation about the resolution at the experiment, the blue (0.0 mm tangential) curve is taken into account. Under the assumption that a modulus of the OFT (optical transfer function) of 0.5 offers high enough contrast, about 12.5 cycles per mm can be resolved. Therefore, the resolution of the telecentric lens as it is implemented at the experiment is $1/(2 \cdot 12.5) = 40\,\mu\text{m}$[15].

[15]The simulation was done by Mr. Platz Andreas from Sill Optics GmbH & Co. KG.

3.8 Imaging the Atomic Cloud

First tests with the Cheetah 110Hz on the experiment were done using the software "Xeneth" delivered with the camera. For these tests, image sequences in low gain and high gain mode were taken. One sequence consists of three images: one image of the atoms, one background-image and one dark image (no illumination). Such an example sequence can be seen in Figure (23). The dark edge in the images (23a) and (23b) is due to the fact that the field of view is larger than the window of the vacuum chamber through which the cloud is imaged. Thus, at the edge there is no 1083 nm illumination light hitting the sensor of the camera.

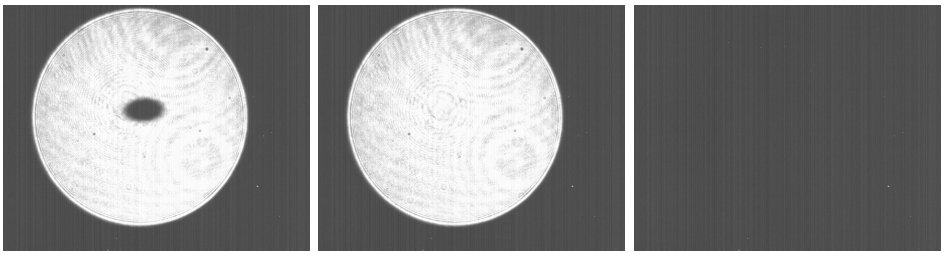

(a) (b) (c)

Figure 23: (23a) shows an image of the atomic cloud done as part of one image sequence. (23b) shows an image of the light that illuminates the atoms, usually denoted as background-image. (23c) is a dark image.

For further investigation, histograms of these test sequences both for high gain and low gain mode were created and can be seen in Figure (24).

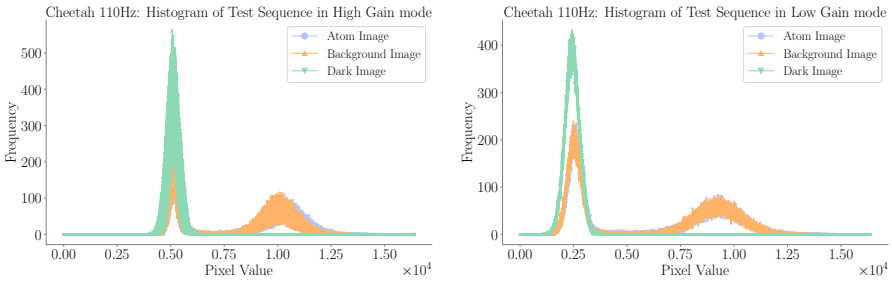

(a) (b)

Figure 24: (24a) shows the histogram of a test sequence taken in high gain mode whereas (24b) shows the histogram of a low gain sequence. When analyzing, two things were noticed: First, when zooming in (see Figure (26)), a pattern of dips appears. Second, as visible in the above graphs, the peaks at low pixel value do not overlap in the histogram.

As already visible in Figure (24b) the peaks at low pixel values, resulting from the dark edge in the images (see Figure (23a) and (23b)), do not overlap in the histograms. In order to get further information of this fact, these peaks were fitted with a Gaussian function, both for the high and low gain sequences. As shown in Figure (25), in both cases the peaks do not overlap. Even though several tests were done, so far no explanation for this effect has been found. The current assumption is that the on-board software corrections of the camera – which can not be fully turned off – depend on the total illumination of the sensor, which differs between those three images.

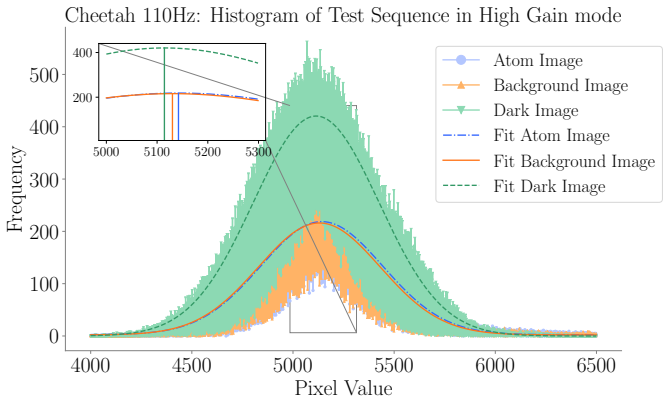

(a)

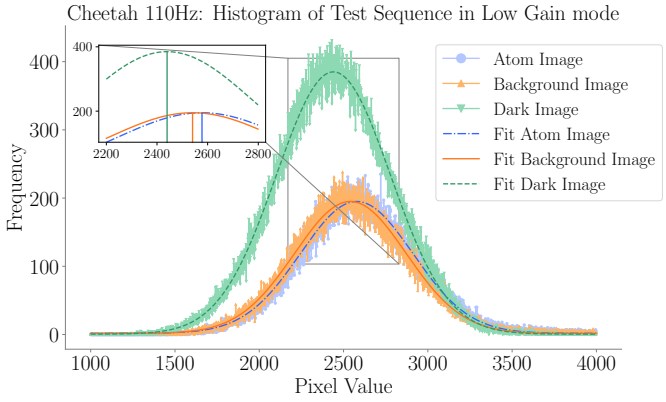

(b)

Figure 25: Investigation of the peaks at low pixel values in the histograms. Those peaks result from the dark edge in the images (see Figure (23a) and (23b)). In both high gain and low gain sequences those peaks do not overlap for the three images of such a test sequence. The shift between the peaks is even larger for the low gain mode, as shown in (25b).

Another effect that appears during investigation of the histograms is a pattern which looks like a smearing out of the histogram, visible in the histograms of the high gain images (see Figure (26a)) but not in the low gain images (see Figure (26b)).

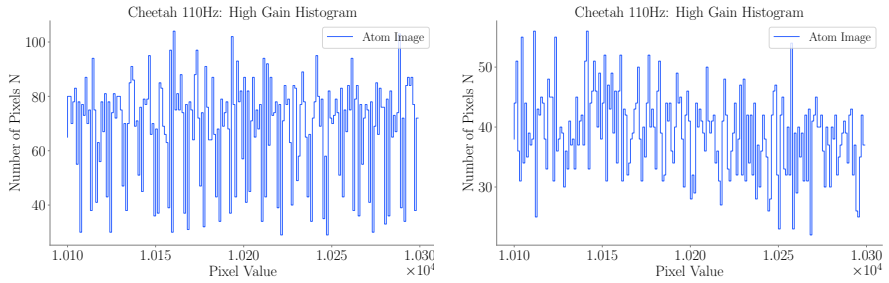

(a) (b)

Figure 26: Pattern of dips arising in the histogram of the high gain images (26a) but not in the low gain images (26b).

In order to investigate this pattern further, the histograms were Fourier transformed. Figure (27) shows the Fourier transformed histogram of a dark image from a sequence taken in high gain mode and one from a low gain sequence respectively. The histogram of the high gain mode shows indeed some pattern of dips occurring with frequency $f = 1/0.115 \approx 8.7$ (in arbitrary units) as revealed by the Fourier transform[16].

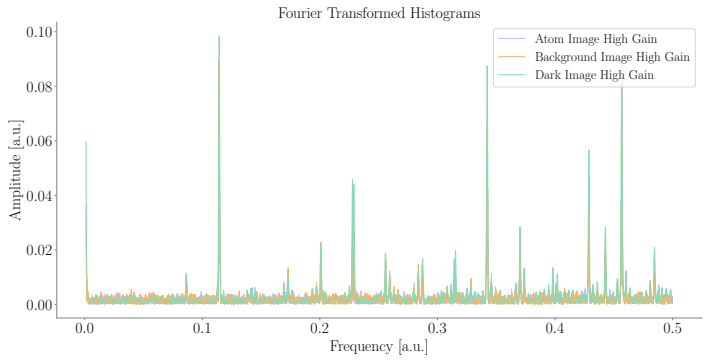

Figure 27: Fourier transformations of the histograms of a test sequence at which all the three images were taken with the Cheetah 110Hz camera in high gain mode. As already expected after Figure (26), the Fourier transform reveals a pattern with frequency $f = 1/0.115 \approx 8.7$ in arbitrary units.

[16] The images taken in low gain mode were analyzed in the same way but, as already supposed from Figure (26b), without any abnormalities.

In order to get a better understanding of this effect, images from the Cheetah 110Hz dark measurements were compared with the dark image of the high gain test sequence. As the first ones were also taken in high gain mode, one would expect to see the same effects. Nevertheless, nothing like that appeared, as revealed in Figure (28).

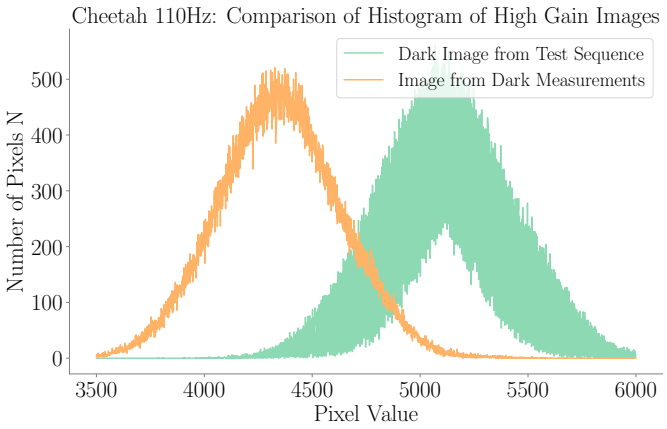

Figure 28: Histograms of a dark image from the test sequence and a dark image of the dark measurements. Exposure times were 150 μs for the first and 110 μs for the latter, which is the reason for the shift with respect to the x-axis between the histograms. The histogram from the dark measurements does not show a pattern like the other one does.

As already mentioned, these first tests were done with the software Xeneth, delivered together with the camera.
In order to gain better understanding and full control over the camera settings, the camera is now accessible via LabVIEW. Since that, none of the above mentioned pattern showed up again. Thus, the current assumption is that this pattern was due to problems with the camera settings in the software Xeneth which were not comprehensibly.

3.9 Summary

After testing four different InGaAs cameras, the Cheetah 110Hz camera was purchased. It offers 14 bits A/D conversion and shows linear noise behavior. Its high quantum efficiency of $\sim 70\%$ in the infrared regime leads to a substantial noise improvement in the absorption images. The new telecentric objective with a magnification of 0.28 shows no obvious distortion effects. This assures that the atomic cloud is correctly magnified, even after longer time of flights where the cloud is at the edge of the field of view. With this improved imaging system, it is not only possible to further investigate the BEC, but also to characterize the dipole trap and gain accuarte knowledge of the properties of the BEC.

Chapter 4 Crossed Optical Dipole Trap

For the further progress and success of this experiment, it is crucial to gain detailed knowledge of the BEC and its properties like size, temperature, chemical potential, mean free path and so on. As the BEC is formed in the crossed optical dipole trap, characterizing and investigating the trap in detail is of huge importance. This investigation can be done using parametric excitation, which is described in more detail in Chapter (4.2).

4.1 Trapping Frequencies

For a single gaussian beam propagating in z-direction the intensity can be written in cylindrical coordinates [44]:

$$I(\rho, z) = I_0 \cdot \left(\frac{w(z)}{w_0}\right)^2 \cdot e^{-2\left(\frac{\rho}{w(z)}\right)^2} , \tag{28}$$

where $w(z)$ is the beam radius and w_0 is the minimal waist radius:

$$w(z) = w_0 \sqrt{1 + \left(\frac{z}{z_R}\right)^2} . \tag{29}$$

The waist radius is related to the Raleigh length z_R:

$$z_R = \frac{\pi}{\lambda} w_0^2 . \tag{30}$$

As the atomic cloud in the dipole trap is expected to be much smaller than the beam waist w_0, the dipole potential $U_{\mathrm{Dip}}(\vec{r}) = \alpha I(\vec{r})$ can be approximated with a second order potential [44]:

$$U_{\mathrm{Dip}}(\vec{r}) = U_{\mathrm{Dip}}(\vec{0}) + \nabla U_{\mathrm{Dip}}(\vec{0})\vec{r} + \frac{1}{2}\vec{r}^{\intercal}\Big(HU_{\mathrm{Dip}}(\vec{0})\Big)\vec{r} + \mathcal{O}(|\vec{r}|^3) , \tag{31}$$

with H being the Hesse matrix. As the first order derivatives vanish at $\vec{r} = \vec{0}$, the above equation simplifies to:

$$U_{\mathrm{Dip}}(\vec{r}) = U_{\mathrm{Dip}}(\vec{0}) + \frac{1}{2}\rho^2 \frac{\partial^2 U_{\mathrm{Dip}}(\vec{r})}{\partial \rho^2}\Big|_{\vec{r}=\vec{0}} + \frac{1}{2} z^2 \frac{\partial^2 U_{\mathrm{Dip}}(\vec{r})}{\partial z^2}\Big|_{\vec{r}=\vec{0}} + \mathcal{O}(|\vec{r}|^3) , \tag{32}$$

where with Equation (28), one finds the following expressions for the second order derivatives:

$$\frac{\partial^2 U_{\mathrm{Dip}}(\vec{r})}{\partial \rho^2}\Big|_{\vec{r}=\vec{0}} = \alpha I_0 \frac{4}{\omega_0^2} \,, \tag{33}$$

$$\frac{\partial^2 U_{\mathrm{Dip}}(\vec{r})}{\partial z^2}\Big|_{\vec{r}=\vec{0}} = \alpha I_0 \frac{2}{z_R^2} \,. \tag{34}$$

With that, the dipole potential can be approximated with:

$$U_{\mathrm{Dip}}(\vec{r}) \approx -\alpha I_0 \Big[1 - 2\Big(\frac{\rho}{\omega_0^2}\Big)^2 - \Big(\frac{z}{z_R^2}\Big)^2\Big] \,, \tag{35}$$

where for helium $\alpha \approx 1.4$ a.u. [45]. In order to get the approximation for a crossed optical dipole trap, where one beam propagates along the x-direction and the other one along the y-direction, the results for each beam are superimposed, with in this case $\rho_1^2 = y^2 + z^2$ and $\rho_2^2 = x^2 + z^2$:

$$U_{\mathrm{Dip}}(\vec{r}) \approx -\alpha I_{0_1}\Big[1 - 2\Big(\frac{y}{\omega_{0_1}^2}\Big)^2 - 2\Big(\frac{z}{\omega_{0_1}^2}\Big)^2 - \Big(\frac{x}{z_{R_1}^2}\Big)^2\Big] \tag{36}$$

$$-\alpha I_{0_2}\Big[1 - 2\Big(\frac{x}{\omega_{0_2}^2}\Big)^2 - 2\Big(\frac{z}{\omega_{0_2}^2}\Big)^2 - \Big(\frac{y}{z_{R_2}^2}\Big)^2\Big] \,. \tag{37}$$

Comparing the above equation with the harmonic potential $U_{\mathrm{harm}} = \frac{1}{2} m(\vec{\omega}\cdot\vec{r})^2$, the trapping frequencies ω_i can be read off:

$$\omega_x = \sqrt{\frac{2\alpha}{m}\Big(\frac{I_{0_1}}{z_{R_1}^2} + 2\frac{I_{0_2}}{\omega_{0_2}^2}\Big)} \,, \tag{38}$$

$$\omega_y = \sqrt{\frac{2\alpha}{m}\Big(\frac{I_{0_2}}{z_{R_2}^2} + 2\frac{I_{0_1}}{\omega_{0_1}^2}\Big)} \,, \tag{39}$$

$$\omega_z = \sqrt{\frac{4\alpha}{m}\Big(\frac{I_{0_1}}{\omega_{0_1}^2} + 2\frac{I_{0_2}}{\omega_{0_2}^2}\Big)} \,. \tag{40}$$

At the experiment, the two beams are supposed to have the same intensity and waist size, meaning that $I_{0_1} \approx I_{0_2}$, $\omega_{0_1} \approx \omega_{0_2}$ and also $z_{R_1} \approx z_{R_2}$. This leads to:

$$2\frac{1}{\omega_0^2} + \frac{1}{z_R^2} = 2\frac{1}{\omega_0^2} + \frac{1}{\big(\frac{\pi}{\lambda}\omega_0^2\big)^2} = 2\frac{1}{\omega_0^2}\Big[1 + \frac{1}{2}\Big(\frac{\lambda}{\pi\omega_0^2}\Big)^2\Big] \approx 2\frac{1}{\omega_0^2} \,. \tag{41}$$

With that, the final simplified expressions for the trapping frequencies at the experiment are:

$$\omega_x = \sqrt{\frac{4\alpha}{m}\frac{I_{0_1}}{\omega_{0_1}^2}}\,, \tag{42}$$

$$\omega_y = \sqrt{\frac{4\alpha}{m}\frac{I_{0_2}}{\omega_{0_2}^2}}\,, \tag{43}$$

$$\omega_z = \sqrt{\omega_x^2 + \omega_y^2}\,. \tag{44}$$

With those expressions, it is possible to rewrite the dipole potential in the harmonic approximation as:

$$U_{\mathrm{Dip}}(\vec{r}) = \frac{1}{2}m\omega_x^2 x^2 + \frac{1}{2}m\omega_y^2 y^2 + \frac{1}{2}m\omega_z^2 z^2 \tag{45}$$

4.2 Parametric Excitation

Parametric excitation is a method which enables measuring the trap frequencies by oscillating the trap depth with an excitation frequency ω_p. This yields to information about size and shape of the trap [46]. Classically, a parametrically driven harmonic oscillator can be described by [33]:

$$\ddot{x} + \beta(t)\dot{x} + \omega_0^2 x = F(t)x\,, \tag{46}$$

where $\beta(t)$ is the damping coefficient, ω_0 is the eigenfrequency of the oscillator and $F(t)$ is an external force which modulates the system. If the system is harmonically modulated, the forcing term has the following form:

$$F(t) = -\omega_0^2 f_0 \sin(\omega_p t)\,, \tag{47}$$

with $f_0\omega_0^2$ being the amplitude of the modulation and ω_p being the frequency of parametric excitation. The maximum amount of energy is pumped into the system in the case of $\omega_p = 2\omega_0$ or at any subharmonic $\frac{2\omega_0}{n}$. In these cases, one speaks about resonant amplification of the oscillating system. In the case of $f_0 \ll 1$, the width of this resonant is given by $f_0\omega_0$. When pumping energy into this system by means of parametric excitation, the atoms in the trap are heated up, which further leads to trap losses. Those trap losses can be measured by absorption imaging. Thus, when the parametric excitation frequency ω_p, for which the trap losses reveal a maximum, is found, the trapping frequency ω_0 is determined.

4.2.1 Experimental Realization

Experimentally, parametric excitation is done by periodic variation of the depth U_0 of the crossed optical dipole trap. The depth is determined by the intensity of the laser beams. Thus, in order to vary the laser intensity of the trap beams, the power of the AOMs is modulated harmonically by sending a sinusoidal RF signal with certain amplitude and frequency - the parametric excitation frequency ω_p. By scanning this frequency and taking absorption images for every frequency, trap losses can be analyzed and the frequency which leads to maximum trap loss can be determined. First, this was done for both trap beams simultaneously, however it was not possible to distinguish which of the measured resonances were assigned to which beam. Thus, the horizontal and the vertical beams were modulated separately and independent of each other.
As seen in Equation (42), the trap frequencies are dependent on the intensity in the respective beam: $\omega \propto \sqrt{I}$. Thus, higher intensity should lead to a higher trap frequency. The intensities of the beams can be regulated directly on the computer via the LabVIEW program: when the atoms are loaded into the dipole trap, cooling is done via evaporation. This means, that the intensity in the trap is lowered until a certain threshold value and atoms which are too hot start to fall out of the trap. This evaporation value can be set to any value between 0 and 1 and determines at the end the intensity in the beam. As already mentioned, the parametric excitation is done by sending an amplitude modulated RF frequency to the AOMs. The peak to peak amplitude of the signal determines how strong the trap is modulated and also influences the width of the resonance.
The measurements done for the horizontal ODT beam can be seen in Figure (29), (30) and (31). In all three measurements, the power of the trap was changed by $\sim 5\%$. This was already enough to see obvious trap losses at two different frequencies. Measurements were done at two different evaporation settings in order to verify that the trap frequencies increase when the intensity in the beam is increased. Further, two different values for the amplitude were investigated in order to verify if the width of the resonance increases by increasing the amplitude. Both from theory expected behaviors of the resonances could be verified with the measurements.
The measurement of the vertical ODT beam was done with an amplitude of $1V_{pp}$, which corresponds to a trap depth modulation of $\sim 11\%$, otherwise no obvious trap losses were visible. The result of the parametric excitation can be seen in Figure (32).

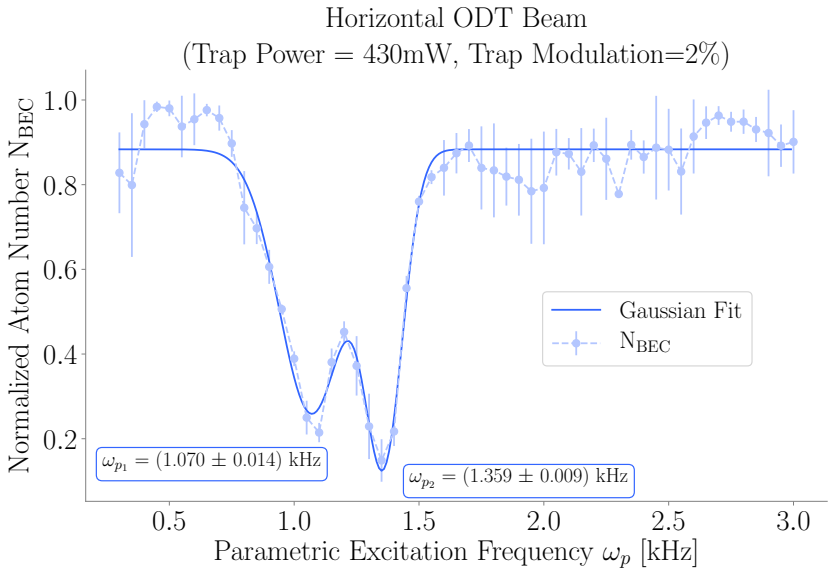

Figure 29: Parametric excitation measurement of the horizontal ODT beam at a trap power of 430 mW and a trap modulation of 2%. Obvious trap losses of $\sim 60 - 70\%$ occur at two different frequencies ω_{p_1} and ω_{p_2}.

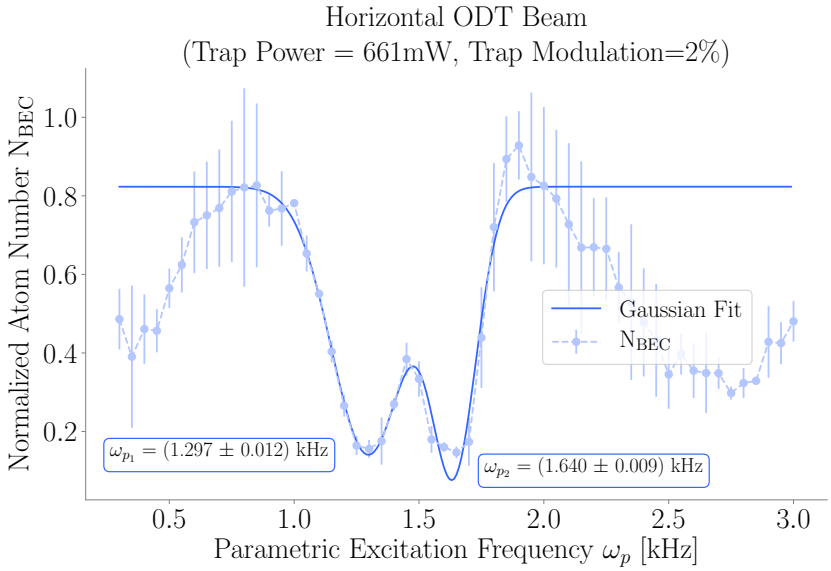

Figure 30: Parametric excitation measurement of the horizontal ODT beam at a trap power of 661 mW and a trap modulation of 2%. As expected, the two resonances shift to higher values when the trap power increases.

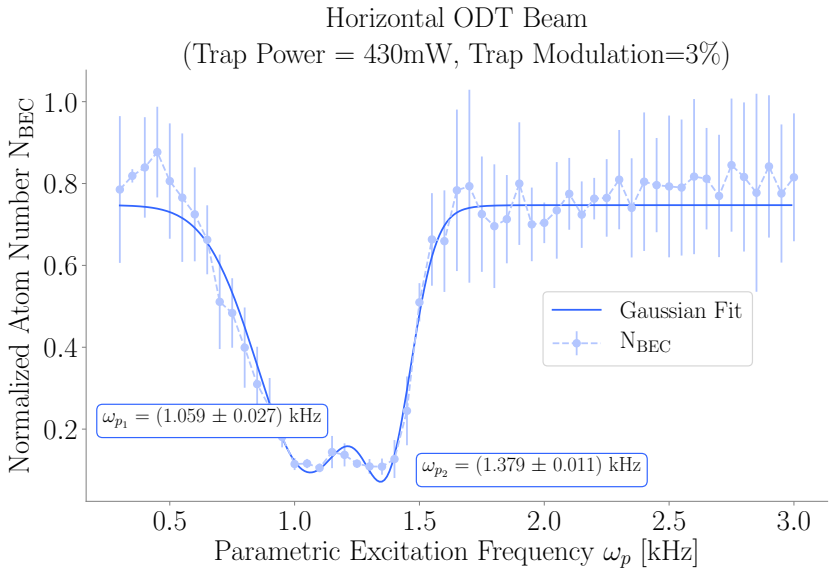

Figure 31: Parametric excitation measurement of the horizontal ODT beam at a trap power of 430 mW and a trap modulation of 3%. The widths of the two resonances are clearly broadened due to the larger modulation. Nevertheless, it is still possible to distinguish the two features.

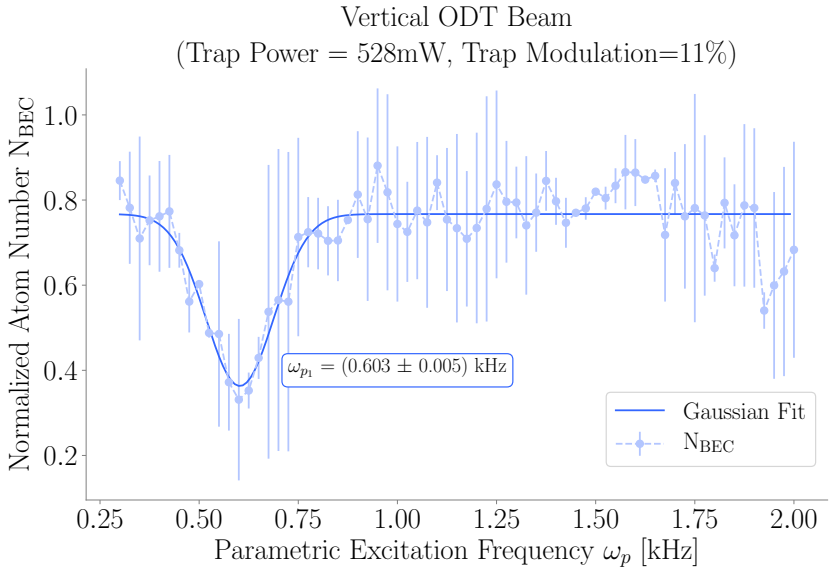

Figure 32: Parametric excitation measurement of the vertical ODT beam at a trap power of 528 mW and a trap modulation of 11%.

The settings for the respective measurement of both trap beams as well as the resulting trap frequencies are listed in Table (2). The errors are uncertainties from the fitting, except for the trap frequency. Here the maximum error was assumed.

	Horizontal ODT Beam			**Vertical ODT Beam**
Trap Power	430 mW	430 mW	661 mW	528 mW
Trap Modulation	2%	3%	2%	11%
Exc. Frequency [Hz]	1070 ± 14 1359 ± 9.0	1059 ± 27 1379 ± 11	1297 ± 12 1640.1 ± 9.0	603.2 ± 5.0
Width [Hz]	120 ± 10 73.4 ± 5.0	207 ± 50 94 ± 18	147 ± 14 90.2 ± 9.0	85.3 ± 7.0
Trap Frequency [Hz]	535.0 ± 7.0 679.5 ± 4.5	529 ± 14 689.5 ± 5.5	648.5 ± 6.0 820.1 ± 4.5	301.5 ± 3.5

Table 2: Results of the parametric excitation measurements for both the horizontal and the vertical optical dipole trap (ODT) beam. For the horizontal beam, measurements were done at two different trap powers and also at two different trap modulations. In all three cases, two trap frequencies could be determined. For the vertical beam, the smallest possible trap power and trap modulation were 528 mW and 11% in order to see a significant decrease in the atom number from which a trap frequency could be deduced.

According to Equation (44), one would expect for the trap frequency in z-direction at a trap power of 430 mW:

$$\omega_z = \sqrt{301.5^2 + 535^2} = 614.11\,\text{Hz} \tag{48}$$

As the measured value is $\omega_z = 679.50$ Hz, this is 65.39 Hz off from the measurement. Even with the assumption of a maximum error for the respective trap frequencies, the combined trap frequency is still off by ~ 57 Hz, as in this case $\omega_z = 620.18$ Hz.
Knowing the trap frequencies gives important information about the trap. With these results, it is now possible to determine more information about the BEC which is created in this trap. Chemical potential, mean free path and density can be calculated with the knowledge about the trap frequencies.

4.3 Parameters of the BEC

As already described in Chapter (3.2.1) a Bose-Einstein condensate can be represented with the Gross-Pitaevski Equation (14). Solving this equation under the Thomas-Fermi approximation leads to the following solution for the density of the BEC [39]:

$$n_{\mathrm{BEC}}(\vec{r}) = \frac{1}{g}\big(\mu - U_{\mathrm{ext}}(\vec{r})\big) \ , \tag{49}$$

with $g = 4\pi\hbar^2 a/m$ being the interaction parameter and μ the chemical potential. In the dipole trap, the external potential $U_{\mathrm{ext}}(\vec{r})$ corresponds to the dipole potential $U_{\mathrm{Dip}}(\vec{r})$ from Equation (45), hence:

$$n_{\mathrm{BEC}}(\vec{r}) = \frac{1}{g}\Big(\mu - \frac{m}{2}\big(\omega_x^2 x^2 + \omega_y^2 y^2 + \omega_z^2 z^2\big)\Big) \ . \tag{50}$$

With that, the Thomas-Fermi radii R_i, the boundaries at which the density becomes zero and therefore define the size of the optical dipole trap, can be defined:

$$0 = \frac{1}{g}\Big(\mu - \frac{m}{2}\sum_{i\in\{x,y,z\}} \omega_i^2 R_i^2\Big) \ . \tag{51}$$

This leads to an expression for the Thomas-Fermi radii R_i (with $i \in \{x, y, z\}$):

$$R_i = \sqrt{\frac{2\mu}{m\omega_i^2}} \ . \tag{52}$$

Knowing the Thomas-Fermi radii also enables determining the number N_{BEC} of condensed atoms in the BEC:

$$N_{\mathrm{BEC}} = \int_0^{R_x}\int_0^{R_y}\int_0^{R_z} n_{\mathrm{BEC}}(\vec{r})\mathrm{d}x\mathrm{d}y\mathrm{d}z \ . \tag{53}$$

This can be simplified by applying a transformation to elliptical coordinates:

$$x = \frac{1}{\omega_x} r\sin\theta\cos\phi \ , \tag{54}$$

$$y = \frac{1}{\omega_y} r\sin\theta\sin\phi \ , \tag{55}$$

$$z = \frac{1}{\omega_z} r\cos\theta \ , \tag{56}$$

with the Jacobian of this transformation being $\frac{1}{\omega_x\omega_y\omega_z} r^2 \sin\theta$. This leads to:

$$N_{\mathrm{BEC}} = \int_0^{2\pi}\int_0^{\pi}\int_0^{\sqrt{2\mu/m}} \mathrm{d}\varphi\mathrm{d}\theta\mathrm{d}r \frac{r^2\sin\theta}{\omega_x\omega_y\omega_z}\frac{m}{2g}\Big(2\frac{\mu}{m} - r^2\Big) \tag{57}$$

$$= 2\pi\frac{m}{g\omega_x\omega_y\omega_z}\int_0^{\sqrt{2\mu/m}} \mathrm{d}r\Big(2r^2\frac{\mu}{m} - r^4\Big) \tag{58}$$

$$= 2\pi\frac{m}{g\omega_x\omega_y\omega_z}\left(\frac{2}{3}\frac{\mu}{m}\Big(\sqrt{2\frac{\mu}{m}}\Big)^3 - \frac{1}{5}\Big(\sqrt{2\frac{\mu}{m}}\Big)^5\right) \tag{59}$$

$$= \frac{4\pi}{15}\frac{m}{g\omega_x\omega_y\omega_z}\Big(2\frac{\mu}{m}\Big)^{5/2} \tag{60}$$

$$= \frac{8\pi}{15}\frac{\mu}{g}\sqrt{\frac{2\mu}{m\omega_x^2}}\sqrt{\frac{2\mu}{m\omega_y^2}}\sqrt{\frac{2\mu}{m\omega_z^2}}\,. \tag{61}$$

It results in an expression for the condensed atom number depending on the Thomas-Fermi radii:

$$N_{\mathrm{BEC}} = \frac{8\pi}{15}\frac{\mu}{g}R_xR_yR_z\,. \tag{62}$$

Further, with Equation (60), the chemical potential μ can be expressed as:

$$\mu = \frac{m}{2}\Big(\frac{15}{4\pi}\frac{g\omega_x\omega_y\omega_z}{m}N_{\mathrm{BEC}}\Big)^{2/5}\,. \tag{63}$$

This is an important result and enables the determination of the chemical potential of the BEC, as the number of atoms in the BEC can be received by fitting the absorption images and the trap frequencies ω_i have been determined with the method of parametric excitation (see Chapter (4.2)).
For calculating the chemical potential of the BEC, the mean atom number of 26 experimental runs was used: $N_{\mathrm{BEC}} = (1.42 \pm 0.15)\cdot 10^6$. With $a = 7.512\cdot 10^{-9}\,\mathrm{m}$ the interaction parameter is $g = 1.58\cdot 10^{-49}\,\mathrm{J\,m^3}$. Thus, the chemical potential can be calculated:

$$\boxed{\mu = (1.5112 \pm 0.0071)\cdot 10^{-30}\,\mathrm{J}} \tag{64}$$

From Equation (52), it is now possible to calculate the three different Thomas Fermi radii:

$$\boxed{R_x = (70.76 \pm 0.99)\,\mu\mathrm{m}} \tag{65}$$

$$\boxed{R_y = (39.88 \pm 0.69)\,\mu\mathrm{m}} \tag{66}$$

$$\boxed{R_z = (31.40 \pm 0.37)\,\mu\mathrm{m}} \tag{67}$$

By knowing the Thomas Fermi radii, the volume of the BEC can be calculated to:

$$\boxed{V = (371\,154 \pm 16\,000)\,\mu\mathrm{m}^3} \tag{68}$$

By assuming constant density over this volume, the average density of the BEC can be calculated:

$$\boxed{n = (3.82 \pm 0.58)\,\mu\mathrm{m}^{-3}} \tag{69}$$

According to $\lambda_{\mathrm{mean}} = (8\pi a^2 n)^{-1}$, with $a = 7.512 \cdot 10^{-9}\,\mathrm{m}$, the mean free path of an atom in the condensate is:

$$\boxed{\lambda_{\mathrm{mean}} = (184.42 \pm 0.22)\,\mu\mathrm{m}} \tag{70}$$

Chapter 5 Conclusion and Outlook

In conclusion, in the framework of this master thesis the absorption imaging system was improved, offering better possibilities for more detailed investigations of the atomic cloud. A new camera for imaging the cloud was purchased. The Cheetah 110Hz is a camera with an indium-gallium-arsenide (InGaAs) sensor from Xenics. It shows 14 bits analog to digital conversion and a linear dark noise behavior. Its quantum efficiency of $\sim 70\%$ compared to the 1% of the previous EMCCD camera in the infrared regime leads to a huge noise improvement in the final absorption images.
Further, the imaging lens improved as the new telecentric lens provides better resolution and does not show visible distortion effects. This assures that the size of the atomic cloud is determined correctly, also when the cloud is imaged at the edge of the field of view. In a few months, a second objective will be available. It will offer the possibility to choose between the magnifications: either the current $M = 0.28$ lens or the new one with $M = 1.85$. The improvements of the absorption system enabled investigation of the atomic cloud and the dipole trap, in which the BEC is created. The trap frequencies of the crossed optical dipole trap were measured for the first time. This is an important step, as these frequencies give information about the size and shape of the trap. With that knowledge, accurate information about density, size, chemical potential and mean free path of the BEC were gained for the first time. This information is also important for the further progress of the experiment and will allow better control and understanding of the dipole trap and therefore also of the BEC produced in this trap.

Chapter A Appendix

A.1 Expansion of a Thermal Cloud: Free Fall

In order to receive a term for the number of atoms in a thermal cloud, the starting point is the initial probability distribution of finding an atom in the phase space volume element $(x_0, y_0, z_0, v_{x0}, v_{y0}, v_{z0})$, which is given by a product of the probability distribution in space $g(i_0, \sigma_0)$ with the probability distribution in velocity space $g(v_{i_0}, \sigma_v)$:

$$n(x_0, y_0, z_0, v_{x0}, v_{y0}, v_{z0}) = \prod_{i \in \{x,y,z\}} g(i_0, \sigma_0) g(v_{i_0}, \sigma_v)\,, \tag{71}$$

with the general form for a Gaussian distribution:

$$g(x, \sigma) = (2\pi\sigma^2)^{-1/2} \exp(-x^2/(2\sigma^2))\,. \tag{72}$$

Under the assumption of starting with a spherically symmetric cloud, all Gaussian radii σ_0 can assumed to be the same (starting with a non-spherical cloud would lead to three different Gaussian radii). The Gaussian radius of the velocity distribution is related to the temperature T of the cloud and the mass m of the atoms via:

$$\sigma_v^2 = \frac{k_B T}{m}\,, \tag{73}$$

where k_B is Boltzmann's constant.

Assuming free fall of the atomic cloud in z-direction (e.g. after releasing the cloud from a trap), one gets the following expressions for the initial velocities:

$$v_{z0} = \frac{z - z_0}{t} - \frac{1}{2} g t\,, \qquad v_{y0} = \frac{y - y_0}{t}\,, \qquad v_{x0} = \frac{x - x_0}{t}\,. \tag{74}$$

With this, the initial coordinates can be expressed:

$$z_0 = z - v_{z0} t - \frac{1}{2} g t^2\,, \qquad y_0 = v_{y0} t - y\,, \qquad x_0 = v_{x0} t - x\,. \tag{75}$$

Equation (75) can be used to substitute the initial coordinates in Equation (71):

$$n(x,y,z,v_{x0},v_{y0},v_{z0},t) = (2\pi\sigma_0^2)^{-3/2}(2\pi\sigma_v^2)^{-3/2}\exp\Big(-\frac{(z-v_{z0}t-\frac{1}{2}gt^2)^2}{2\sigma_0^2}\Big) \times \exp\Big(-\frac{(v_{y0}t-y)^2}{2\sigma_0^2}\Big)\exp\Big(-\frac{(v_{x0}t-x)^2}{2\sigma_0^2}\Big)\exp\Big(-\frac{v_{z0}^2}{2\sigma_v^2}\Big) \times \exp\Big(-\frac{v_{y0}^2}{2\sigma_v^2}\Big)\exp\Big(-\frac{v_{x0}^2}{2\sigma_v^2}\Big)\,. \tag{76}$$

A first order result for the probability of finding an atom at position (x,y,z) after a time t can be achieved by integrating Equation (76) over the velocities (v_x,v_y,v_z). Under the assumption of a low density (resulting in a low collision probabilty) these velocites can in first order be approximated by the initial velocities, leading to integrals over the latter:

$$n(x,y,z,t) = \int_{-\infty}^{\infty}\int_{-\infty}^{\infty}\int_{-\infty}^{\infty} \mathrm{d}v_{x0}\mathrm{d}v_{y0}\mathrm{d}v_{z0}\, n(x,y,z,v_{x0},v_{y0},v_{z0})\,. \tag{77}$$

In order to keep the overview for the reader, $c = (2\pi\sigma_0^2)^{-1/2}(2\pi\sigma_v^2)^{-1/2}$ is defined and the calculation will firstly be done just in one dimension, namely in z-direction:

$$\begin{aligned} n(z,t) &= c\int_{-\infty}^{\infty}\mathrm{d}v_{z0}\,\exp\Big(-\frac{(z-v_{z0}t-\frac{1}{2}gt^2)^2}{2\sigma_0^2}\Big)\exp\Big(-\frac{v_{z0}^2}{2\sigma_v^2}\Big) \\ &= c\int_{-\infty}^{\infty}\mathrm{d}v_{z0}\,\exp\Big(-\frac{1}{2\sigma_0^2}(z^2+v_{z_0}^2t^2+\frac{1}{2}g^2t^4-2zv_{z_0}t-gzt^2 \\ &\quad + gt^3v_{z_0}) - \frac{v_{z_0}^2}{2\sigma_v^2}\Big) \\ &= c\int_{-\infty}^{\infty}\mathrm{d}v_{z0}\;\exp\Big(-v_{z_0}^2(\frac{t^2}{2\sigma_0^2}+\frac{1}{2\sigma_v^2}) + \frac{v_{z_0}}{2\sigma_v^2}(2zt-gt^3) \\ &\quad - \frac{1}{2\sigma_0^2}(z^2-gzt^2+\frac{1}{4}g^2t^4)\Big)\,. \end{aligned} \tag{78}$$

The above can be further simplified by defining:

$$\sigma_t = \sqrt{\sigma_0^2+\sigma_v^2t^2}\,. \tag{79}$$

$$
\begin{aligned}
n(z,t) &= c \int_{-\infty}^{\infty} \mathrm{d}v_{z0}\ \exp\Big(- v_{z_0}^2 \frac{\sigma_t^2}{2\sigma_0^2\sigma_v^2} + \frac{v_{z_0}}{2\sigma_v^2}(2zt - gt^3) - \frac{1}{2\sigma_0^2}(z - \frac{1}{2}gt^2)^2\Big) \\
&= c\ \exp\Big(- \frac{1}{2\sigma_0^2}(z - \frac{1}{2}gt^2)^2\Big) \int_{-\infty}^{\infty} \mathrm{d}v_{z0}\ \exp\Big(- \frac{\sigma_t^2}{2\sigma_0^2\sigma_v^2}\big(v_{z_0}^2 + \\
&+ \frac{\sigma_v^2 v_{z_0}}{2\sigma_t^2}(2zt - gt^3)\big)\Big) .
\end{aligned} \tag{80}
$$

Completing the square of the last term in Equation (80) leads to:

$$
\begin{aligned}
N(z,t) &= c\ \exp\Big(- \frac{1}{2\sigma_0^2}(z - \frac{1}{2}gt^2)^2\Big) \exp\Big(\frac{\sigma_v^2 t^2}{2\sigma_0^2\sigma_t^2}(z - \frac{1}{2}gt^2)^2\Big) \\
&\int_{-\infty}^{\infty} \mathrm{d}v_{z0}\ \exp\Big(- \frac{\sigma_t^2}{4\sigma_0^2\sigma_v^2}\big(v_{z_0}^2 + \frac{\sigma_v^2}{2\sigma_t^2}(2zt - gt^3)\big)^2\Big) \\
&= c\ \exp\Big(- (z - \frac{1}{2}gt^2)^2 \frac{\sigma_t^2 - \sigma_v^2 t^2}{2\sigma_0^2\sigma_t^2}\Big) \int_{-\infty}^{\infty} \mathrm{d}u\ \exp\Big(- \frac{\sigma_t^2}{4\sigma_0^2\sigma_v^2}(u)^2\Big) \\
&= c\ \exp\Big(- \frac{1}{2\sigma_t^2}(z - \frac{1}{2}gt^2)^2\Big) \int_{-\infty}^{\infty} \mathrm{d}u\ \exp\Big(- \frac{\sigma_t^2}{4\sigma_0^2\sigma_v^2}(u)^2\Big) ,
\end{aligned} \tag{81}
$$

where in the second last line the substitution method was used to simplify the integral further and in the very last line, Equation (79) was used to express σ_0 in terms of σ_t and σ_v. Finally, the integral can be solved by using the standard result for a Gaussian integral:

$$
\int_{-\infty}^{\infty} \mathrm{d}x\ \exp(-ax^2) = \sqrt{\frac{\pi}{2a}} , \tag{82}
$$

leading to:

$$
\begin{aligned}
n(z,t) &= (2\pi\sigma_0^2)^{-1/2}(2\pi\sigma_v^2)^{-1/2}\Big(\frac{4\pi\sigma_0^2\sigma_v^2}{2\sigma_t^2}\Big)^{1/2} \exp\Big(- \frac{1}{2\sigma_t^2}(z - \frac{1}{2}gt^2)^2\Big) \\
&= (2\pi\sigma_t^2)^{-1/2} \exp\Big(- \frac{1}{2\sigma_t^2}(z - \frac{1}{2}gt^2)^2\Big) .
\end{aligned} \tag{83}
$$

Written in a more compact form, the final result is achieved:

$$
n(z,t) = g(z - \frac{1}{2}gt^2, \sigma_t) . \tag{84}
$$

For the other coordinates, the calculation can be done analogously. Putting it all together, one ends up with:

$$
n(x,y,z,t) = g(x,\sigma_t)g(y,\sigma_t)g(z - \frac{1}{2}gt^2, \sigma_t) . \tag{85}
$$

A.2 Datasheet of the Cheetah 110Hz Camera

Xenics
Infrared Solutions

Imagine the invisible

Scientific

Cheetah-640CL TE3

High resolution
cooled InGaAs-camera

Cheetah-640CL TE3 for low light level imaging and spectroscopy

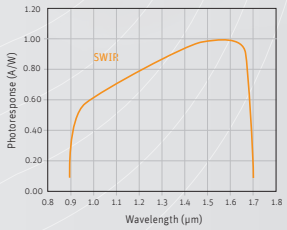

The Cheetah-640CL TE3 camera is a high resolution, compact infrared camera, equipped with a dedicated low noise InGaAs detector array working from 0.9 µm up to 1.7 µm.

With its TE3 cooled sensor and water cooled camerahead, the Cheetah-640CL TE3 is a highly sensitive camera achieving ultra low dark current at long integration times. It offers you an excellent measurement tool to image low light levels in the SWIR range such as for semiconductor failure analysis or for luminescence spectroscopy applications.

The Cheetah- 640CL TE3 is delivered with a software development kit which offers direct access to various camera settings and allows easy integration with your own CameraLink image grabbing system.

Designed for use in

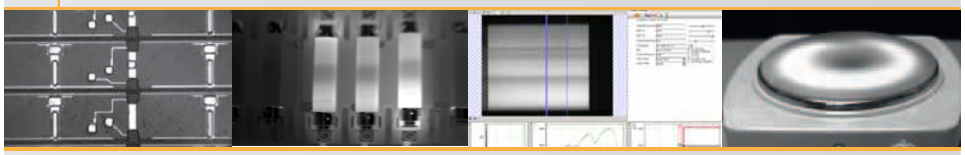

- Semiconductor analysis
- Reliability study
- Research & Development
- Failure detection

Applications

- Fluorescence
- R&D (SWIR range)
- Emission microscopy
- Semiconductor failure analysis
- Low light level imaging spectroscopy: raman, emission, photoluminescense, absorbance

Benefits & Features

- High resolution
- Low dark current
- Flexible GUI and SDK
- No need for LN2 cooling
- Spectrograph compatible
- High quantum efficiency (> 80 %)

Broad range of accessories available to simplify your research

Lens & filter options

Inputs

Software

- Xeneth advanced
- Xeneth SDK

Outputs

Specifications

Array Specifications	Cheetah-640CL TE3
Array type	InGaAs
Spectral band	0.9 to 1.7 µm
# Pixels	640 x 512
Pixel pitch	20 µm
Array cooling	TE3-cooled
Pixel operability	> 99%
Camera Specifications	**Cheetah-640CL TE3**
Lens (included)	
Focal length	25 mm f/1.4
Optical interface	C-Mount, spectrometer holes
Imaging performance	
Frame rate (full frame)	110 Hz
Integration type	Snapshot
Window of Interest	Minimum size 32 x 4 pixels
A to D conversion resolution	14 bit
Interfaces	
Camera control	CamerLink (LVDS voltage levels)
Image acquisition	Base CL (14 bit)
Trigger	3.3 V CMOS levels (trigger in & out)
Graphical User Interface (GUI)	Xeneth Advanced
Power requirements	
Power consumption	Max. 20 W
Power supply	12 V
Physical characteristics	
Camera cooling	Water cooling
Ambient operating temperature	0 °C to 50 °C
Dimensions	140 W x 135 H x 90 L mm
Weight camera head	2 kg

Product selector guide

Part number	TE Cooling	Digital output interface	Frame rate (Hz)	ADC
XEN-000271	TE3	CameraLink	110	14 bit

www.xenics.com
www.sinfrared.com

Xenics Headquarters
Ambachtenlaan 44, BE-3001 Leuven, Belgium
T +32 16 38 99 00 • sales@xenics.com

Xenics
Infrared Solutions

ISO 9001:2008 certified

References

[1] A. Einstein, B. Podolsky, and N. Rosen. Can Quantum-Mechanical Description of Physical Reality Be Considered Complete? Physical Review, 47(10):777–780, 1935.

[2] E. Schrödinger and M. Born. Discussion of Probability Relations between Separated Systems. Mathematical Proceedings of the Cambridge Philosophical Society, 31(04):555, 1935.

[3] D. Bohm and Y. Aharonov. Discussion of Experimental Proof for the Paradox of Einstein, Rosen, and Podolsky. Physical Review, 108(4):1070–1076, 1957.

[4] J. S. Bell. On the Einstein Podolsky Rosen paradox. Physical Review Letters, 1(3):195–200, 1964.

[5] A. Perrin, H. Chang, V. Krachmalnicoff, M. Schellekens, D. Boiron, A. Aspect, and C. I. Westbrook. Observation of atom pairs in spontaneous four-wave mixing of two colliding Bose-Einstein condensates. Physical Review Letters, 99(15):150405, 2007.

[6] S. Bose. Plancks Gesetz und Lichtquantenhypothese. Z. Physik (Zeitschrift für Physik), 26(1):178–181, 1924.

[7] A. Einstein. Quantentheorie des idealen einatomigen Gases. Sitzungsberichte der preussischen Akademie der Wissenschaften, 1924.

[8] M. H. Anderson, J. R. Ensher, M. R. Matthews, C. E. Wieman, and E. A. Cornell. Observation of Bose-Einstein condensation in a dilute atomic vapor. Science (New York, N.Y.), 269(5221):198–201, 1995.

[9] K. B. Davis, M. O. Mewes, M. R. Andrews, N. J. van Druten, D. S. Durfee, D. M. Kurn, and W. Ketterle. Bose-Einstein condensation in a gas of sodium atoms. Physical Review Letters, 75(22):3969–3973, 1995.

[10] S. F. Pereira, J. Léonard, J. Wang, C. J. Barrelet, F. Perales, E. Rasel, C. S. Unnikrishnan, M. Leduc, and C. Cohen-Tannoudji. Bose-Einstein condensation of metastable helium. Physical Review Letters, 86(16):3459–3462, 2001.

[11] A. Robert, O. Sirjean, A. Browaeys, J. Poupard, S. Nowak, D. Boiron, C. I. Westbrook, and A. Aspect. A Bose-Einstein condensate of metastable atoms. Science (New York, N.Y.), 292(5516):461–464, 2001.

[12] J. Kofler, M. Singh, M. Ebner, M. Keller, M. Kotyrba, and A. Zeilinger. Einstein-Podolsky-Rosen correlations from colliding Bose-Einstein condensates. Physical Review A, 86(3):195, 2012.

[13] A. J. Ferris, M. K. Olsen, and M. J. Davis. Atomic entanglement generation and detection via degenerate four-wave mixing of a Bose-Einstein condensate in an optical lattice. Physical Review A, 79(4), 2009.

[14] J. M. Vogels, K. Xu, and W. Ketterle. Generation of macroscopic pair-correlated atomic beams by four-wave mixing in Bose-Einstein condensates. Physical Review Letters, 89(2):020401, 2002.

[15] Z. Y. Ou, X. Y. Zou, L. J. Wang, and L. Mandel. Observation of nonlocal interference in separated photon channels. Physical Review Letters, 65(3):321–324, 1990.

[16] Z. Y. Ou, S. F. Pereira, H. J. Kimble, and K. C. Peng. Realization of the Einstein-Podolsky-Rosen paradox for continuous variables. Physical Review Letters, 68(25):3663–3666, 1992.

[17] K. V. Kheruntsyan, J-C Jaskula, P. Deuar, M. Bonneau, G. B. Partridge, J. Ruaudel, R. Lopes, D. Boiron, and C. I. Westbrook. Violation of the Cauchy-Schwarz inequality with matter waves. Physical Review Letters, 108(26):260401, 2012.

[18] M. Keller, M. Kotyrba, F. Leupold, M. Singh, M. Ebner, and A. Zeilinger. Bose-Einstein condensate of metastable helium for quantum correlation experiments. Physical Review A, 90(6), 2014.

[19] G. Modugno, G. Ferrari, G. Roati, R. J. Brecha, A. Simoni, and M. Inguscio. Bose-Einstein condensation of potassium atoms by sympathetic cooling. Science (New York, N.Y.), 294(5545):1320–1322, 2001.

[20] C. C. Bradley, C. A. Sackett, and R. G. Hulet. Bose-Einstein Condensation of Lithium: Observation of Limited Condensate Number. Physical Review Letters, 78(6):985–989, 1997.

[21] R. S. van Dyck, S. L. Zafonte, S. van Liew, D. B. Pinegar, and P. B. Schwinberg. Ultraprecise atomic mass measurement of the alpha particle and 4He. Physical Review Letters, 92(22):220802, 2004.

[22] S. S. Hodgman, R. G. Dall, L. J. Byron, K. G. H. Baldwin, S. J. Buckman, and A. G. Truscott. Metastable helium: A new determination of the longest atomic excited-state lifetime. Physical Review Letters, 103(5):053002, 2009.

[23] F. M. Penning. Über Ionisation durch Metastabile Atome. Die Naturwissenschaften 15, (no. 40):818, 1927.

[24] S. Moal, M. Portier, J. Kim, J. Dugué, U. D. Rapol, M. Leduc, and C. Cohen-Tannoudji. Accurate determination of the scattering length of metastable helium atoms using dark resonances between atoms and exotic molecules. Physical Review Letters, 96(2):023203, 2006.

[25] M. Ebner. Development of a metastable helium BEC as a platform for experiments with EPR-entangled matter waves. Ph.D. Thesis, University of Vienna, 2012.

[26] Kotyrba M. Bose-Einstein condensation of metastable helium-4 for quantum entanglement experiments. Ph.D. Thesis, University of Vienna, 2015.

[27] A. Aspect, N. Vansteenkiste, R. Kaiser, H. Haberland, and M. Karrais. Preparation of a pure intense beam of metastable helium by laser cooling. Chemical Physics, 145(2):307–315, 1990.

[28] C. J. Dedman, J. Nes, T. M. Hanna, R. G. Dall, K. G. H. Baldwin, and A. G. Truscott. Optimum design and construction of a Zeeman slower for use with a magneto-optic trap. Review of Scientific Instruments, 75(12):5136–5142, 2004.

[29] N. Herschbach, P. J. J. Tol, W. Hogervorst, and W. Vassen. Suppression of Penning ionization by spin polarization of cold He(23S) atoms. Physical Review A, 61(5):89, 2000.

[30] C. V. Sukumar and D. M. Brink. Spin-flip transitions in a magnetic trap. Physical Review A, 56(3):2451–2454, 1997.

[31] O. J. Luiten, M. W. Reynolds, and J. T. M. Walraven. Kinetic theory of the evaporative cooling of a trapped gas. Physical Review A, 53(1):381–389, 1996.

[32] R. Grimm, M. Weidemüller, and Y. B. Ovchinnikov. Optical dipole traps for neutral atoms. Advances In Atomic, Molecular, and Optical Physics, Volume 42, p.95-170, 2000.

[33] S. Chaudhuri, S. Roy, and C. S. Unnikrishnan. Evaporative Cooling of Atoms to Quantum Degeneracy in an Optical Dipole Trap. Journal of Physics: Conference Series, 80:012036, 2007.

[34] A. Ashkin. Trapping of Atoms by Resonance Radiation Pressure. Physical Review Letters, 40 (729), 1978.

[35] K. M. O'Hara. Optical trapping and evaporative cooling of fermionic atoms. Ph.D. Thesis, Duke University 2000.

[36] P. J. J. Tol. Trapping and Evaporative Cooling of Metastable Helium. Ph.D. Thesis, Vrije Universiteit Amsterdam, 2005.

[37] T. M. Brzozowski, M. Maczynska, M. Zawada, J. Zachorowski, and W. Gawlik. Time-of-flight measurement of the temperature of cold atoms for short trap-probe beam distances. Journal of Optics B: Quantum and Semiclassical Optics, 4(1):62–66, 2002.

[38] C. Pethick and H. Smith. Bose-Einstein condensation in dilute gases. Cambridge University Press, Cambridge, second edition, 2008.

[39] F. Dalfovo, S. Giorgini, L. P. Pitaevskii, and S. Stringari. Theory of Bose-Einstein condensation in trapped gases. Reviews of Modern Physics, 71(3):463–512, 1999.

[40] Y. Takeda, A. Sasaki, Y. Imamura, and T. Takagi. Electron mobility and energy gap of In0.53Ga0.47As on InP substrate. Journal of Applied Physics, 47(12):5405–5408, 1976.

[41] W. Drexler and J. G. Fujimoto. Optical Coherence Tomography: Technology and Applications. Biological and Medical Physics, Biomedical Engineering. Springer, Berlin Heidelberg, 2008.

[42] M. Laikin. Lens design. Optical engineering, Volume 72. Dekker, New York, third edition, 2001.

[43] R. G. Driggers. Encyclopedia of Optical Engineering: Vol. 1 Abe-Las. Dekker, New York, 2003.

[44] W. Gunton. The Loading and Storage of Li and Rb in an Optical Dipole Trap. Bachelor Thesis, University of British Columbia, Vancouver, 2009.

[45] M. Masili and A. F. Starace. Static and dynamic dipole polarizability of the helium atom using wave functions involving logarithmic terms. Physical Review A, 68(1):661, 2003.

[46] S. Balik, A. L. Win, and M. D. Havey. Imaging-based Parametric Resonance in an Optical Dipole Atom Trap. Physical Review A, 80, 023404, 2009.